Fiber Depolymerization: Fracture, Fragments, Vanishing Times and Stochastics in Sickle Hemoglobin

Jiang Cheng Wang[*], Suzanna Kwong[*], Frank A. Ferrone[†], Matthew S. Turner[‡], and Robin W. Briehl[*]

[*]Department of Physiology and Biophysics, Albert Einstein College of Medicine, Bronx, New York; [†]Department of Physics, Drexel University, Philadelphia, Pennsylvania; [‡]Department of Physics, University of Warwick, Coventry, United Kingdom

Abstract

The well-characterized rates, mechanisms and stochastics of nucleation-dependent polymerization of deoxyhemoglobin S (HbS) are important in governing whether or not vaso-occlusive sickle cell crises will occur. The less well studied kinetics of depolymerization may also be important, for example in achieving full dissolution of polymers in the lungs, in resolution of crises and/or in minimizing gelation-induced cellular damage. We examine depolymerization by microscopic observations on depolymerizing HbS fibers, by Monte Carlo simulations and by analytical characterization of the mechanisms. We show that fibers fracture. Experimental scatter of rates is consistent with stochastic features of the analytical model and Monte Carlo results. We derive a model for the distribution of vanishing times and also show the distribution of fracture-dependent fiber fragment lengths and its time dependence. We describe differences between depolymerization of single fibers and bundles and propose models for bundle dissolution. Our basic model can be extended to dissolution of gels containing many fibers and is also applicable to other reversible linear polymers that dissolve by random fracture and end-depolymerization. Under the model, conditions in which residual HbS polymers exist and facilitate repolymerization and thus pathology can be defined; while for normal polymers requiring cyclic polymerization and depolymerization for function, conditions for rapid cycling due to residual aggregates can be identified.

Introduction

The aim of this study is to discern and characterize new features of the depolymerization of HbS fibers. These are: (i) the time a fiber requires to vanish fully and the stochastic nature and distribution of the vanishing time; (ii) the distribution of fiber fragment lengths as ligand-induced fracture breaks the fibers and as the fragments shorten; (iii) the effects of formation of fiber bundles on depolymerization mechanism and rates; (iv) the relations between depolymerization of single fibers and depolymerization of gels that contain many fibers.

Unlike thoroughly studied nucleation-dependent polymerization (1-4), the mechanism of depolymerization is only partially characterized and its contributions to pathogenesis and its avoidance are not known and have been little examined.

The relevance of the polymerization and gelation of deoxyHbS, the initiating event in sickle cell disease, to pathogenesis lies in manifold effects: contributions to microvascular obstruction, red cell and endothelial damage, and anemia; and in the cascades of multi-factorial pathological events, including cellular adhesion, red cell dehydration, states of hypercoagulability and other factors. In

respect to the direct effect of red cell rigidification that promotes vaso-occlusion, polymerization kinetics have a central role: if the nucleation-dependent delay time is longer than the time needed for transit of red cells through the microvasculature, the propensity for vaso-occlusion will be lessened; conversely, if the delay is shorter, it predisposes to obstruction (3-5).

In contrast to the highly successful double nucleation model for polymerization (2), *previous studies of many aspects of depolymerization (7-15) have not yet led to a complete model for its fundamental molecular mechanisms and rates,* and its relevance to clinical pathology has not been defined. We hypothesize at least three ways in which depolymerization rates may be important. (i) If full depolymerization does not occur in the few seconds that red cells spend in the oxygenating conditions of the lungs, residual polymer will pass into the systemic circulation, thereby eliminating the nucleation-dependent portion of the delay time and predisposing to vaso-occlusion. *Mozzarelli et al (4) have demonstrated the generation of rapid polymerization in red cells in the presence of small amounts of residual polymer.* (ii) Rapid depolymerization may help in resolution of sickle cell crises. (iii) Slow depolymerization may increase the likelihood and/or extent of red cell damage and also the extent of endothelial damage arising from the presence of rigid, grossly deformed, cells. Huang et al (16) have made an important advance by showing that sickle red cell deformability is not restored for several seconds after exposure to oxygenation or CO. Our current work looks at the same problem from the perspective of depolymerization kinetics and mechanisms, which lie at the root of restoration of deformability.

We begin with our model for HbS fiber depolymerization (17,18). It invokes two processes, depolymerization of fibers and fiber fragments at their ends by loss of monomers, and ligand-induced fracture of fibers that creates fragments. These processes lead to two kinds of depolymerization: slow, ligand-independent, loss of monomers (i.e. 64,500 dalton tetramers) from initial fiber ends without fracture; and ligand binding-dependent 'fading' in which fibers appear to dissolve rapidly along their entire lengths. We attributed the 'fading' appearance to limited light microscopic resolution that could not resolve fractures. 'Fading' for single (i.e. 14-stranded (19,20)) fibers is well modeled by a fracture and depolymerization-at-fragment-ends mechanism (18). Pure end-depolymerization (i.e. only at the initial fiber ends) is slow and proceeds at about 0.75 μm/sec at each end (17). In it, the time for complete fiber dissolution is proportional to fiber length. In contrast, 'fading' is more rapid because of the presence of new fragments and ends, and occurs over a wide range of rates depending on the frequency of fracture, which itself depends on ligand concentration. Full dissolution can occur in small fractions of a second and the time required is independent of fiber length. Because of the great difference in rates, whether dissolution is achieved by depolymerization only at initial fiber ends or by the combined fracture and end-depolymerization of fragments (hereafter designated "fracture/end") may be important for minimization of pathophysiological effects.

Our model (18) developed an analytic, mean-field, approach encompassing both pure end-depolymerization and the fracture/end mechanism, and identifies a large regime over which the latter operates. The model predicts that fracture/end dissolution progresses as an exponential in time squared, $exp(-(t/\tau)^2)$, where $\tau = 1/\sqrt{k\,q}$ is a characteristic time, k is the end-depolymerization rate and q is the fracture rate per unit fiber length. Based on Monte Carlo simulations, the amount of polymer remaining exhibits stochastic properties in the form of variations of remaining polymer mass as a function of time.

In the present work we examine depolymerization in 3 ways that provide synergistic evidence: with a new theoretical model, by Monte Carlo simulations, and by experimental observations of HbS fibers. Under the analytic model and in Monte Carlo simulations, and consistent with experimental data, depolymerization is a stochastic process. Our model describes the stochastics in a pathologically relevant way, as the distribution of fiber vanishing times. It also characterizes the distribution of fiber fragment lengths during depolymerization. We also propose extensions of the model to encompass the effects of fiber bundle formation and to address dissolution of HbS gels.

Depolymerization: Mechanisms and Models

Model for depolymerization with random breakage

We derive equations for depolymerization in a new way that characterizes fiber vanishing times, stochastics and fragment length distributions. The steps in the derivation follow.

1. Random breaks without depolymerization. For a very long initial fiber *that has undergone random fracture*, and neglecting end-effects, we choose a segment at random. The probability that it belongs to the class of segments of length exactly x units (e.g. molecules or layers) scales as,

$$r(x) = (1-\alpha)^x \alpha^2 \tag{1}$$

where α is the breakage probability at any unit *(mathematical symbols are defined in Table I)*. For $\alpha << 1$, as is usually the case, and thus using only the first order term and normalizing, $n(x)$ and $p(x)$, the number and probability of segments of length x are, respectively,

$$n(x) = \alpha\, N\, e^{-\alpha x} \tag{2}$$

$$p(x) = \alpha\, e^{-\alpha x} \tag{3}$$

where N is the total number of fragments. (The second order term is negligible as long as $\alpha x << 1$, i.e. $x << 1/\alpha$). The mass distribution, $\varphi(x)$ is,

$$\varphi(x) = x\, n(x) = x\, \alpha\, N\, e^{-\alpha x} \tag{4}$$

Total fiber mass (length, L_o) is,

$$L_0 = \int_0^\infty x\, n(x) dx = \frac{N}{\alpha} \tag{5}$$

so that,

$$n(x) = \alpha^2 \, L_0 \, e^{-\alpha x} \tag{6}$$

$$\varphi(x) = x \, \alpha^2 \, L_0 \, e^{-\alpha x} \tag{7}$$

2. Continuing breakage at rate *q* per unit length. We set $\alpha=qt$ and *thus express n and φ as functions of time*,

$$n(x,t) = q \, t \, N(t) \, e^{-q x t} \tag{8}$$

$$\varphi(x,t) = x \, q \, t \, N(t) \, e^{-q x t} \tag{9}$$

$$N(t) = q \, t \, L_0 \tag{10}$$

3. Continuing breakage with fiber shortening. Shortening of fragments at rate *k* at each end is now introduced. The change in *n(x,t)* with time is,

$$\frac{\partial n}{\partial t} = 2k \frac{\partial n}{\partial x} - q \, x \, n + 2q \int_x^\infty n \, dx \tag{11}$$

where the first term on the right represents the effect of fibers of length $x+dx$ shortening to increase *n(x)* and of length *x* shortening to decrease *n(x)*; the second term represents the effect of breakage of fibers of length *x* on *n(x)*; and the third term the effect of breakage of fibers longer than *x*. Solving equation (11) and defining a characteristic time (as in Turner et al, 2006), $\tau = 1/\sqrt{k \, q}$

$$n(x,t) = q \, t \, N(t) \, e^{-q x t} = (q \, t)^2 \, L_0 \, e^{-q x t - (t/\tau)^2} \tag{12}$$

$$\varphi(x,t) = x \, (q \, t)^2 \, L_0 \, e^{-q x t - (t/\tau)^2} \tag{13}$$

$$N(t) = q \, t \, L_0 \, e^{-(t/\tau)^2} \tag{14}$$

$$L(t) = \frac{N(t)}{q \, t} = L_0 \, e^{-(t/\tau)^2} \tag{15}$$

where *N(t)* and *L(t)* are remaining number of fragments and fiber length (mass), respectively.

4. Stochastic distribution of vanishing times. We now cast equation (14) in a dimensionless form to derive a generalized expression for the distribution of vanishing times. We also replace L_o with $L_i=L_o-2kt$, to allow for the effects of shortening at the two initial fiber ends. Using $s \equiv t/\tau$, $A_o \equiv L_o \sqrt{q/k}$ and $A=(L_o-2kt)\sqrt{q/k} = A_o-2s$ in equation (14), $\overline{N}(s)$, the mean number of fragments remaining is,

$$\overline{N}(s) = (A_0 - 2s)s\, e^{-s^2} \tag{16}$$

We are interested in onset of the condition *N=0*, which defines the loss of all polymer, and its probabilistic dependence on $\overline{N}$. Thus, we seek the probability *P(s,A$_o$,0)* that there is no fiber at time *s*; and its derivative, *∂P/∂s=p(s,A$_o$,0)*, which is the distribution function for vanishing times.

We model the system by conceptually extracting random sections of an extremely long fiber to create an ensemble of fibers of initial length L_o, which may be long but still vastly shorter than the initial hypothetical fiber. We assume that, when the fiber is largely depolymerized and there are few fragments left, the presence of any given fragment is independent of other fragments and all fragments are much smaller than *L*. Then, given the mean number of fragments remaining, $\overline{N}$, we use a Poisson distribution to obtain the probability that *N=0*,

$$P(s, A,0) = e^{-\overline{N}}\ \overline{N}^{0}/0! = e^{-(A_0-2s)s\,e^{-s^2}} \tag{17}$$

Differentiating to obtain $\partial P(s,A_o,0)/\partial s \equiv p(s,A_o,0)$,

$$p(s, A_0,0) = A_0 e^{-(A_0-2s)s\,e^{-s^2}}\ e^{-s^2}\,[(2s^2-1) - 4s(s^2-1)/A_0] \tag{18}$$

is the desired distribution function for vanishing times.

Equation (18) is valid in the regime of the fracture/end mechanism providing *k* is small enough and/or L_o is long enough and *q* rapid enough that dissolution depends primarily on creation of fragments and their end-depolymerization, not on end-depolymerization at the 2 initial fiber ends. The measure of this is the dimensionless parameter, A_o. The time that would be required for pure end-depolymerization to dissolve the fiber, $L_o/2k$, should be substantially greater than the characteristic time, τ, i.e. $(L_o/2)\sqrt{q/k} = A_o/2 > 1$; *this assures that depolymerization at the original two ends contributes negligibly to the vanishing time. A somewhat more stringent criterion that addresses the regime over which the Poisson approximation is justified requires that the amount of fiber remaining shall constitute only a small fraction of L_o-2kt, the length of fiber that would remain if dissolution were purely by end-depolymerization. This criterion assures that the remaining fragments are present independently. Replacing L_o by L_o-kt, the criterion becomes $A_o/2$-s>1, where s represents the time range of applicability. This modification constrains s as well as A_o. For low A_o it can exclude the beginning to the distribution, where s is relatively large. The validity of analyses under equation (18) and its regime of applicability as it depends on A_o can be affirmed by comparison to results of Monte Carlo simulations (below). s≥2 assures that less than 2% of polymer remains, but our Monte Carlo results indicate that a less stringent criterion, s≥1.5 and perhaps lower values as well also suffice and result in little error, depending on the value of A_o.*

Figure 1a shows a series of curves that plot *p(s,A$_o$,0)* in the most general way, as a function of *s*, for different values of A_o in the regime of large A_o. Thus, each curve reports the probability of vanishing as a function of the ratio of vanishing time to characteristic time and can be applied to different sets of units (length and time) and values *(L,q,k)* provided A_o is kept the same. If *k* and L_o are held constant, as in the figure, A_o scales as $\sqrt{q}$ so that large A_o indicates faster depolymerization.

That faster curves lie to the right of slower ones on the reduced time, *s*, axis depends on the different abscissa scalings as $\tau = 1/\sqrt{k\,q}$ changes with A_o. Plotted against time, *t*, faster curves would lie to the left. (An example of a less general plot in true time, *t*, is shown below, figure 5). Figure 1b plots the curves of figure 1a semi-logarithmically to show the approximately 2-fold width of the vanishing time distributions if the low probability tails of the distribution are included. *Figure 1 also shows that the distributions are skewed to the right and hence not gaussian.*

5. Distribution of fragment lengths. Differentiation of equation (12) gives,

$$\frac{\partial \ln(n)}{\partial x} = -q\,t \tag{19}$$

$$\frac{\partial \ln(n)}{\partial t} = \frac{2}{t} - q\,x - \frac{2t}{\tau^2} \tag{20}$$

and shows (figure 2a) that the distribution of fragment lengths is a decreasing exponential that becomes steeper with time. Figure 2b illustrates changes in the number of fibers within a unit length range over time. The population at each length reaches a maximum and then decreases, as is also the case for the total number of fragments (equation (14)). The maximum occurs earlier for long fragments than for short ones. Long fragments become extremely rare not long after depolymerization commences.

Depolymerization of fiber bundles

Single HbS fibers commonly aggregate laterally to form stable fiber bundles (21-24). We propose models for depolymerization of bundles that fall into three classes, schematized in figure 3. (a) A bundle might depolymerize as a concerted unit, with all fibers fracturing at the same site simultaneously, and with all fibers within a bundle fragment undergoing end-depolymerization at the same rate, schematized in figure 3a. The single fiber model is then applicable without modification other than a possible change in the dependence of fracture and/or end-depolymerization rate on ligand concentration (which governs fracture rate (18)). (b) Each fiber might undergo random fracture and end-depolymerization independently (but at the same mean rates) while remaining as part of a bundle. Depolymerization would then progress as it does for single fibers in free solution, and vanishing times for each single fiber would also be unaffected. But fracture of the bundle would not occur as rapidly as for a single fiber because overlap of gaps in each single fiber would be uncommon, as shown in figure 3b. (c) Finally, fracture rates for each single fiber could depend on the presence or absence of neighboring fibers. For example, a fiber in the center of a bundle and not exposed to solution might be protected against fracture until one or more surrounding fibers in the radially adjacent region depolymerized, schematized in figure 3c. In this kind of model, depolymerization will be slower than for types (a) and (b) and, as for type (b), continuity will be maintained for a longer time than for a single fiber.

Monte Carlo Simulations of Dissolution Stochastics and Fiber Fragment Lengths

We use simulations for single fibers to test our model-based equations for the stochastics of vanishing time and the distribution of fragment lengths. For each simulation, the intrinsic structural

and kinetic parameters that suffice to characterize the system are L_o, q, and k or, alternatively, L_o, τ, and k.

Stochastics: Vanishing Times

Figure 4 shows the results of 10,550 simulations that produce a distribution of vanishing times that conforms well to the distribution predicted by equation (18). The agreement between the theoretical equation and Monte Carlo results justifies the assumption used, that the last few remaining fragments can be treated as being present randomly and independently, and that application of a Poisson distribution is therefore warranted. The analytical and Monte Carlo data are essentially superposed even at times in which more than a few fragments remain and a discernible fraction of polymer remains. The figure also shows the cumulative probability (P) that vanishing has occurred by a given time, t, and the fraction of polymer remaining, L/L_o.

Figure 5a shows Monte Carlo distributions of vanishing times for a range of fracture rates. As q increases, vanishing time is shorter and the absolute width of the distribution decreases greatly. But, shown in the semilogarithmic plot of figure 5b, increasing q is still associated with a narrowing distribution of relative vanishing times.

Stochastics: Characteristic Times

Turning from vanishing to characteristic times, figure 6 shows a simulated distribution of characteristic times, τ, (figure 6a) along with the distribution of vanishing times in the same simulation (figure 6b). The vanishing times are necessarily longer, by a factor of about 2, but the shapes of the distributions are similar and right-skewed.

Skewing of Distributions: Vanishing and Characteristic Times

Figure 4 shows right skewing of the theoretical curve and the superposed simulated depolymerizations for vanishing time, affirmed over a range of rates in figures 1 and 5, by theory and simulation, respectively. The simulations in figure 6 show the similarity of skewing of characteristic time (skewness 0.94) to that for vanishing times (1.06). The vanishing time distribution is relatively wider: the ratio of standard deviation to mean vanishing time, $\Delta t_v/t_v$ is 0.18 compared to that for characteristic time, $\Delta\tau/\tau$=0.11. For this simulation, in which A_o=10, the ratio of these two values, 1.64, lies close to the value predicted, $\sqrt{\ln(A_0)}$ =1.52, by the approximate analysis in our mean field theory (18).

Fragment Length Distributions

Figure 7 shows the results of Monte Carlo simulations for fragment length distribution and mass distribution at two times during a depolymerization. The length distribution is *a decreasing* exponential (figure 7a). It becomes steeper with time, and conforms well to the analytical model, equation (12). The mass distributions (figure 7b) also conform to analytical predictions (equation (13)). They demonstrate the predominance of remaining mass in the shorter fragments as dissolution progresses.

Experimental Results

Depolymerization of HbS Fibers: Fracture and Thinning

We examined HbS fibers experimentally to ascertain if depolymerization is consistent with the basic features of our model as expressed analytically and simulated in Monte Carlo results: fiber fracture, progress curves, and stochastics. Figure 8 shows a series of frames obtained using video-enhanced DIC microscopy. The fiber was created by photolysis of COHbS. Dissolution was commenced by shifting the long, narrow, fiber-containing, photolysis spot slightly to the side of the fiber, thus providing new free CO that diffuses quickly to the fiber and induces dissolution without the need to recruit solution CO from a large distance. Frame (a) shows the fiber before the photolysis spot was shifted and frame (b) shows it shortly after the spot shift, but before any depolymerization can be detected. In (c) image contrast begins to decrease and in (d) the image has faded significantly. This continues in (e) and a short gap appears, indicated by an arrow and enlarged in figure 9, as well as uneven fading in other locations. This becomes more marked in (f). In (g) little fiber remains and there are a number of gaps, after which, in (h), no fiber can be detected visually.

Figure 10a shows the progress curve of dissolution based on the average gray scale values of the darkest pixels along the whole fiber length as a function of time. It provides a guide to the events of fracture, fading of the image seen in figure 8, and the analysis in figure 10b. The circle is placed at the time of frame (e), at which the first evidence of fracture appears in figure 10b and (at the same position) in video frame (e) of figure 8 (indicated by an arrow).

In figure 10b we identify the location of the darkest 5-pixel diameter region in each fiber cross-section (i.e. column of pixels perpendicular to the fiber). Initially, these locations form a continuous line co-linear with the fiber, as in the trace in frame (a). In (e), the line shows a single sharp deviation where it ceases to be co-linear with the fiber, the darkest pixel groups lying at a distance from the fiber. In (f) and (g) more deviations occur randomly on either side of the fiber, but there are still intact sections of the fiber. The deviations are consistent with fiber fracture and gaps at those locations: because there is no fiber, there are no dark pixels at that site and the darkest pixels in a normal direction are randomly located. Finally, in (h), lacking discernible fiber, the darkest pixel groups are all randomly located.

Depolymerization Stochastics

In figure 11, we show the progress curve of a depolymerizing fiber (11a) and then, for purpose of analysis, divide it into 55 contiguous sections, each 10 pixels wide in the fiber direction (pixel size is 44 nm in the sample plane). Gray scale values of the DIC image (see legend and Methods) are used to generate progress curves of dissolution for each section of the fiber. *The distribution of characteristic times, τ, is shown in (11b), while (11c) shows randomness in the distribution of τ along the length of the fiber. In figure 11d the progress curves for two of the sections are selected to show the distinct differences in rate of depolymerization.*

Table II summarizes results from all fibers examined. The fibers were prepared under CO, with pCO (partial pressure of CO) in the range of 0.2 to 0.8 atmosphere. The fiber pictured in figures 8 and 9 and analyzed in figures 10 and 11 is #7 in the table. All fibers showed fractures as judged by pixel gray scales (as in figure 10b), and in many visible breaks as in figure 8 could also be discerned. All showed scatter in rates of depolymerization when they were examined by sections, as in figure 11. The table shows the extent of scatter, $\Delta\tau$, relative to τ. *The table includes depolymerization induced by shifting of the photolytic spot and that induced by total extinction of photolysis. The latter method is more likely to suffer from diffusion limitation, especially at low pCO, because of the need to recruit CO from a long distance (see Methods).*

Dependence of Depolymerization on pCO

Figure 12 shows that characteristic depolymerization times, τ, exhibit an inverse 2.34 power dependence on pCO. Because $\tau^2=1/qk$ and k changes little or not at all with pCO (17), q scales as the approximate 4.7 power of pCO, reaffirming the cooperative nature of the dependence of fracture on CO binding (18). This result shows the cooperativity to be 50% greater than previously measured (18); this is due to the use of the spot-shift method that avoids the diffusion limitation that occurs when CO is recruited from a large distance.

Discussion

Relevance of HbS Fiber Depolymerization to Sickle Cell Disease

Sickle cell gels dissolve under the oxygenating conditions in the lungs. Rates of dissolution depend on numerous factors, most notably the intrinsic rate at which individual fibers dissolve, but probably also other factors in gel structure including the extent and nature of non-covalent interfiber cross-links, the formation of fiber bundles and perhaps other time-dependent alterations of structure. The completeness of depolymerization is likely to be an important factor in pathogenesis: if the 1-3 seconds red cells spend in the oxygenating conditions of the lungs, and perhaps the additional seconds in the arterial circulation prior to reaching the systemic microvasculature, are not sufficient to dissolve all polymer, the protective delay time will be shortened and a new gelation will be facilitated. Depolymerization rates may also affect resolution of vaso-occlusion and the *extent of red cell membrane and other damage that HbS gels inflict*.

That hypoxemia can exist in sickle cell disease is well established. It may arise from overall hypoventilation *(as may occur due to pain and splinting)*, from regional inhomogeneity of ventilation/perfusion ratios or from local atelectasis. It may be associated with sleep apnea. In order to analyze the rates and mechanisms of depolymerization in the lungs, pulmonary function has to be related to the kinetics of depolymerization, which the present study endeavors to characterize. CO, because its extent of liganding to hemoglobin can be photolytically modulated, is a useful model for oxygen. It should model end-depolymerization rates well because they are ligand-independent, the presence of CO serving only to prevent repolymerization of molecules leaving fiber ends. CO in principle serves as a model for mechanisms of fracture, but the ligand-binding equilibria and kinetics are different from those of oxygen, so that *quantitative* translation of ligand partial pressures cannot be made. But once liganding has occurred, the induction of fracture and

kinetics of depolymerization are likely to be the same for CO and oxygen, because they induce the same R-T conformational change in hemoglobin.

The depolymerizations we observe, with characteristic times ranging from fractions of a second to a few seconds are somewhat shorter than the times needed for restoration of sickle red cell deformability reported by Huang et al (16). But the two sets of results are consistent because 37% of polymer still remains at time τ under the fracture/end mechanism and vanishing does not occur until significantly later (figure 6). For this comparison, we use the characteristic time rather than the vanishing time, which cannot be detected by deformability measurements. Using our previous measurement, *k=0.75* μm/s (per end) (17), pure end-depolymerization of an 8 μm fiber will require about 5 sec, which is not much longer than the times at which Huang et al (16) observed restoration of cell deformability in response to ligands (oxygen or CO). Therefore, in the absence of a significant fracture rate, depolymerization is not likely to be achieved even in the absence of pulmonary disease. Hence, the boundary between conditions under which there remains some pure end-depolymerization and conditions under which it is absent and all fibers undergo fracture and more rapid dissolution is significant.

We can relate this condition to our experimental results. We assume a characteristic time of about 1 sec, in the range of figure 12, and k=0.75, so that $q=1/k\tau^2=1.33$ *fractures per second per micron and, for an 8 mμ fiber spanning a red cell,* $A_o=L_o\sqrt{q/k}=9.2$. *This produces slower vanishing times than the right-most simulated curve in figure 5b, for which* $A_o=20$, *and is therefore not sufficient to avoid the passage of some residual polymer through the lungs. (This calculation can also be made from the theoretical curves in figure 1.) The applicability of this estimate, based on CO-dependent fracture, to pathophysiology and oxygen-induced fracture remains to be determined. However, the similarly of oxygen and CO-dependent recovery of cell shape demonstrated by Huang et al (16) suggests that there may not be great differences. In respect to end-depolymerization, it is ligand-independent, ligand serving only to prevent repolymerization of dissociated molecules (17). Thus, once liganding of solution hemoglobin is achieved, end-depolymerization is unaffected by ligand concentration.*

We conclude that *in vivo* rates may not take full advantage of the fracture/end mechanism and hence changes in local conditions that enhance fracture could be of benefit. Because *q* exhibits an approximately 4.7 power dependence on ligand concentration, relatively small improvements in oxygenation in the lungs might provide major benefit in achieving fiber dissolution.

In addition to their importance for the role of the lungs in sickle cell disease, the mechanism and rates of HbS fiber depolymerization are of interest because they may be relevant to depolymerization of other linear polymers. Our model has general features that are potentially applicable to other biological systems.

A Model for Depolymerization

The present work and its antecedents (17,18) provide a basic model for depolymerization. It encompasses non-cooperative, ligand-independent, loss of HbS monomers from fiber ends, and fiber fracture resulting from cooperative liganding and nucleation of fracture sites. End-

depolymerization alone is slow, but when combined with fracture in an end/fracture mechanism of dissolution, rapid.

Stochastics. *Because the combined fracture/end mechanism includes random fracture, we anticipate that kinetics will exhibit stochastic properties. The conclusion that depolymerization is stochastic rests on a number of interrelated lines of evidence. i) Our model, which is consistent with previous experimental observations on dissolution rates and sites and with the presence of fractured fibers in electron micrographs (17, 18), predicts stochastic behavior. ii) Monte Carlo simulations exhibit the stochastics that theory predicts. It then remains to consider experimental evidence presented here. iii) Observed in real time, fibers fracture spontaneously and apparently randomly in time and location. iv) Different sections of a fiber depolymerize at different rates as judged by gray scale-based measurements as well as visual impression. v) Shapes of the distribution of characteristic times of sections of a fiber are consistent with Monte Carlo simulations. While none of these lines of evidence proves stochastic behavior, taken together and with the theory they argue in favor of such behavior. Here we elaborate on iv) and v.*

iv) The results obtained by dividing each fiber into sections for the purpose of analysis are presented in Table II. The Table shows the standard deviations of characteristic times, $\Delta\tau$, for the different fiber sections. This scatter depends on two principal factors: stochastic behavior dependent on random fracture; and scatter deriving from noise in pixel dark scale readings. To assay the extent to which $\Delta\tau$ arises from each of these sources, we compared the experimental data with simulations in which we added random gaussian to simulated depolymerization progress curves. The simulations in the presence of noise in figure 13 show that $\Delta\tau/\tau$, the fractional range of τ, is less in figure 13a, in which there is no fracture and depolymerization itself (i.e. before addition of noise) conforms to a deterministic $\exp(-(t/\tau)^2)$ than in 13b, in which the depolymerization consists of a simulation that includes random fracture and has an average form $\exp(-(t/\tau)^2)$. The level of noise introduced in both parts, 0.2 over the full scale of fractional depolymerization (from 1 to 0), corresponds to the observed gray scale scatter of a section of fiber prior to the beginning of depolymerization. For spot-shift experiments, values of $\Delta\tau/\tau$, averaging 0.175, in Table II are all greater than the 0.088 for that level of noise in the deterministic simulation of figure 13b and similar to the value of 0.139 for the simulation that includes stochastic fracture in 13b. Thus, the experimental values of $\Delta\tau/\tau$ cannot be wholly explained by pixel noise. It is necessary to invoke stochastics of the depolymerization process. The same relationship exists for full photolytic extinction, where the average $\Delta\tau/\tau$ is 0.192. We can come to the same conclusion if we allow for fiber to fiber differences in noise. The last column in Table II shows the ratio $(\Delta\tau/\tau)/\nu$, where ④ is the measured noise for each fiber. For experimental fibers and for simulated fracturing fibers in the upper (simulated fracture) half of Table III, this ratio is significantly greater than it is for fibers without fractures in the lower half of Table III.

Two additional causes, one artifact, one based on depolymerization itself, may contribute to the excess $\Delta\tau/\tau$ for some fibers even over that in simulations with fracture in studies in the presence of pixel-dependent noise. (a) The fibers are slightly bent, so that some parts are nearer than others (by up to 1μm) to the source of CO outside the illuminated spot when the spot is shifted or extinguished. This might produce a diffusion-dependent artifact and an increase in $\Delta\tau$. (b) In analysis of fiber depolymerization by sections the mean number of fractures per section (calculated as fragment length times q, with $q=1/(k\tau^2)$) until vanishing is less than 1 for slow depolymerization

(low pCO). Thus, some fragments vanish only because neighboring sections that do fracture generate depolymerization that crosses into the section that does not fracture. This precludes analysis of the non-fracturing section under the basic model. However, it does generate correlated scatter of depolymerization times in sections that are close together. It may therefore produce systematic patterns in plots of τ against position on fiber such that τ values in neighboring sections may be similar. But, unlike diffusion-dependent effects, this contribution to a systematic pattern does reflect intrinsic fiber stochastics and therefore would not alter a conclusion that stochastics do exist. We conclude that the observed variation in depolymerization rates in different portions of a fiber is consistent with and is necessary to conclude that there are true stochastics, but by itself does not yet conclusively demonstrate stochastics because of possible diffusion artifacts. Hence we estimate the magnitude of a diffusion artifact and its effect in Methods (CO Diffusion), below. We conclude that it is not likely to invalidate the conclusion that the observed variation in τ requires the presence of stochastics; the variation in τ is not fully explained by pixel-dependent noise or diffusion artifact and therefore does provide evidence for stochastic fiber dissolution.

The conclusion that a $\Delta\tau/\tau$ higher than that for a deterministic simulation demonstrates the existence of stochastics can be extended over a range of noise levels, as shown in Table III. This Table reports the ratio $(\Delta\tau/\tau)/\nu$, where, for simulations, ν is the standard deviation of the added gaussian noise; and for experimental data it is the standard deviation of fiber gray scale prior to depolymerization. Using this method, simulated $(\Delta\tau/\tau)/\nu$ is about 0.46 for deterministic fibers independent of noise level, while it is greater in the presence of simulated fracture(Table III) and also in experimental fibers (Table II).

v) In respect to shapes of the distributions of vanishing times and τ shown in figures 1, 4, 5, 6, 12 and 13, they are not gaussian and are right skewed. We use the extent of skewing to compare simulations that include random fracture with those based on deterministic progress curves. Figure 13 exemplifies this difference. The skewing is much greater for fracture-based simulations. The presence of even more marked skewing in the absence of noise is demonstrated in figure 6. Our experimental data include only about 55 sections in the progress curves. Thus, the right skewing seen in figure 11b is not itself statistically significant nor is the right skewing seen in almost all other fibers. Therefore, our experimental observation that right skewing is present in almost all distributions of 55 sections is consistent with the model, but it cannot exclude the null hypothesis with high probability because of the limited number of sections in the distribution for each fiber and the intrinsic variability of skewing.

Based on the diverse lines of evidence and this analysis, we conclude the depolymerization times are stochastically distributed as a consequence of cooperative, ligand-dependent, nucleation of fiber fracture. When it is desired to ascertain the time at which the last residual fiber vanishes, this randomness must be taken into account. The situation parallels that for polymerization, in which cooperative formation of nucleating aggregates generates random delay times (1-3, 25, 26).

Fiber fragment lengths. The present model also characterizes the distribution of fragment lengths and its changes during depolymerization as a decreasing exponential that becomes steeper with time. Thus, the number of long fragments decreases more rapidly than the number of short ones, a fact that may be beneficial because long fibers are more likely to generate gel rigidity.

Fiber fracture. Our previous evidence that fiber fracture occurs during depolymerization and is integral in the mechanism consisted of observations of fragments resulting from dilution as seen by electron microscopy, and the success of our earlier model invoking fracture in rationalizing observed rates of depolymerization (17, 18). In the present work we show by direct observations in real time that fibers fracture during ligand-induced depolymerization. This, and the conformity of our new fracture-based model to Monte Carlo results, further support the existence and basic role of fracture.

Fiber thinning or fracture? A central question for a depolymerization model is whether the fiber is fracturing, whether it is becoming thinner without breaking, or whether it is doing both and if so in what sequence. Fracture is required in our model for a single fiber (above and in Turner et al, (18)). Thinning is not encompassed in the *quantitative* model. The *experimental* problem lies in distinguishing between many fractures with very small gaps that cannot be resolved microscopically and true thinning while the fiber remains continuous. These distinctions are analyzed in figures 8-10 using pixel gray scales.

Figure 8 shows fading of the fiber image with time both before and after frame (e), where the first break occurs. The absence of breaks before frame (e), at which time the fiber is already fading, indicates that the fading must represent thinning without fracture. Similarly, in frame (f) there are few breaks while the remainder of the fiber continues to fade. The clear identification of these few fractures implies that the remainder of the fiber is free of fracture. Hence, the fading of the image must be ascribed to true thinning. Although not *encompassed* by our model for single fibers, it is consistent with the existence of a fiber bundle, modeled in figure 3: eventually, when depolymerization proceeds substantially and the image has partially faded, a gap through the entire bundle develops at one, and then many locations, as schematized in figure 3b (or 3c at a later time than shown in the scheme).

Under our previous model (17, 18), true thinning of fibers without fracture was assumed not to exist even though the video images of fibers were consistent with it as well as with the fracture model. Our present observations confirm that *fractures exist by inspection of images and by gray scale analyses*, but also show fading of images in the absence of fracture. Thus, the previous model, which assumed the existence of only a single fiber, requires modification. The resolution of the problem lies in the existence of fiber bundles.

Modifications and Extensions of the Depolymerization Model

Fiber Bundles. Present results show that depolymerization can progress with fiber fading while fibers remain continuous, as judged by absence of visible fractures over significant lengths of time and spatial fluctuations that are correlated over long lengths. *Therefore, an extension of our quantitative model is needed. We do not undertake this here, but such a model must take into account bundle formation that results in a marked decrease in the rate of gap formation.* We have previously observed (21) that one member of a fiber bundle can grow alongside its mates and thus make the fiber thicken progressively along its length. Here we propose that the opposite, depolymerizing, event can also occur.

Under such a model, fiber bundles will retain rigidity longer than an equal mass of single fibers whether or not they depolymerize as rapidly as single fibers. Because fibers readily, indeed usually, form bundles (21-23) that are thermodynamically stable (24), bundling could contribute to pathology by virtue of increased difficulty of dissolution as well as by any effects it has on gel rigidity itself. In our observations on gels, fibers can spontaneously form bundles by touching and zippering together over the course of time (21, 22). Thus, rapid reversal of gelation may confer benefits by precluding the existence of gels that *anneal and may be* increasingly difficult to dissolve.

Application to HbS Gels

In order to assay the probability that polymer remaining when gels dissolve will promote vaso-occlusion, the distribution of vanishing times for a gel is needed. This can be expected to depend on gel structure and diffusion of ligand into the gel interior. Here we show that gels *per se*, by virtue of number of fibers, have longer vanishing times than a fiber does. Equation (17) provides the cumulative probability that a specific fiber has vanished by time *s*. Hence, the probability that all *g* identical fibers in a gel will have vanished at time *s* is,

$$P_g(s, A_0, 0) = (P(s, A_0, 0))^g = e^{-g A s e^{-s^2}} \tag{21}$$

To achieve total dissolution of all fibers in a gel with high probability, *s* has to be higher than is necessary to assure dissolution of a single fiber. Additionally, because only a small fraction of cells need polymerize to initiate vaso-occlusion, the pathologically critical value of *s* that would preclude vaso-occlusion is even higher.

For a gel with *g* identical fibers to exhibit the same probability of total vanishing as seen with one fiber,

$$e^{-g A s_g e^{-s_g^2}} = e^{-A s_1 e^{-s_1^2}} \tag{22}$$

where the subscripts on s, *g* and *1,* indicate gel and single fiber, respectively. Then,

$$s_g^2 - s_1^2 - \ln(\frac{s_g}{s_1}) = \ln(g) \tag{23}$$

Thus, if we assume 30% of 20 mM (heme) is gelled in an 80 $(\mu m)^3$ red cell, the total single fiber length (for a 14-stranded fiber with 63Å layer repeat (3, 19, 20)) in the cell is about 130,000 μm or 16,000 8 μm fibers. With $g=16{,}000$ and $s_1=2$, then $s_g=3.8$. Thus, the presence of a gel with many fibers significantly increases the time needed to induce vanishing of the last fiber.

If residual polymers occur, each may generate a separate gel domain. Hence, the number of polymers remaining contributes to determination of gel structure and hence the shape and rheological effects of affected red cells. As we have done for $N=0$, equation (17) can be applied with $N>0$ to derive probability distributions for the presence of 1 or more residual fragments. The analysis, however, like that for $N=0$, is limited to times in which little polymer remains and the

presence of individual fragments can be treated as independent events. *The potential for different numbers of residual fragments may be pathologically significant: each residual fiber fragment can give rise to a separate gel domain. More domains will result in faster polymerization and in a multi-domain gel rather than one consisting of a single large domain. The rheological properties as well as the rates of formation properties of different domain structures are likely to be different.*

It should be noted that the conclusion that gels or very long fibers require longer to depolymerize than individual fibers does not contradict our conclusion that dissolution rates under the fracture/end model are independent of fiber length. The apparent contradiction is resolved by noting that independence of length only applies to a normalized distribution and mean rates, and neglects stochastics. When scaled to the actual number of fibers, the tails become longer and the number of fibers with vanishing times in those regions increases. Additionally, fiber lengths have no effect only if end effects are neglected. While they may be negligible in many circumstances, in principle they remain and have significant effects for short fibers, especially with slow fracture rates.

Methods

Simulations

Monte Carlo simulations were carried out on Lotus spreadsheets or with MatLab7. Random gaussian noise was generated in MatLab7 with a Ziggurat algorithm.

Preparations

HbS was purified chromatographically on DE-52 as previously described (27). Samples were deoxygenated with 50 mM sodium dithionite in an anaerobic glove bag containing CO (as desired in the range of 30% to 80%). Slides were prepared in the glove bag and sealed anaerobically with Mount-Quik (Daido Sangyo Co., Ltd).

Individual fibers were isolated from HbS gels as previously (17, 23, 27) using selective photolysis of COHbS to dissolve all except the desired fiber. Total HbS concentrations were 16.0 mM (in heme). Photolysis was achieved with epi-illumination at 436 nm by a mercury arc.

Depolymerization

Depolymerization was induced in two ways. (i) Once a fiber was isolated, depolymerization was induced by shifting the long, narrow (8 μm wide) photolytic spot a distance of 10 μm to one side of the fiber (17) so that the fiber was no longer subject to epi-illumination and therefore dissolved (the spot-shift method). This method provides CO quickly from the newly photolyzed region and thus minimizes diffusion limitation. (ii) Depolymerization was induced by total extinction of photolytic epi-illumination (the epi-off method). Dissolution times by this method are somewhat slower because CO has to be recruited from a large distance. *The former method is superior for obtaining true values of τ because the precise amount of CO needed is made available in close proximity to the fiber and does not have to be recruited from afar.*

Pixel Gray Scales

8-bit pixel gray scales were obtained as the difference between observed gray scale values and background for each pixel. The mean background level was obtained from serial video frames after a fiber had fully dissolved. The temporal noise for a single pixel was measured as 3.5 gray scales so that the standard error of the mean for a strip of 10 pixels (parallel with the fiber), used for figure 11, is approximately 1.1 in gray scale. In figure 10b, 5-pixel diameter regions were used, so that the error is about 0.8 gray scale. The aim of the measurements *in figure 10b* was not to obtain a gray scale value *per se*, but rather to discern the difference between dark pixels representing fiber and*, where fiber had dissolved,* much brighter ones representing background. Pixel averaging was done in order to avoid errors that might occur if a single or a few, possibly aberrant, pixels were used.

Two procedures were used to evaluate fiber fading due to dissolution. (a) In figure 10a, the darkest pixels at each fiber location in its 556 pixel length were averaged over the full fiber length for each time frame. Thus, the average course of depolymerization as expressed in fading was obtained. (b) For figure 11b, the aim was to characterize individual, 10 pixel long, sections of the fiber. Therefore, the noise problem was greater. We used a different method to evaluate progress in these sections. Instead of using the darkest pixels, we measured all pixels in the 10 pixel section of the fiber and obtained an average gray scale for each 10 pixel row in the dark and bright rows parallel to the fiber that are produced by DIC imaging. We then obtained the mean deviation for each row (above or below background) and summed their absolute values across (transverse to) the fiber; thus both the bright and dark pixels contributed to the final value.

These methods provide measures of the mass of polymer present. They discern rates of loss and fractures clearly if the gaps are sufficiently large. But, because of the complex roots of gray scale values in interference-based DIC images, the relation between dark scale and mass need not be linear. Thus, *shapes of gray scale progress curves may not be precise reflections of fiber mass present. But comparative values for sections of fibers observed in the same way, as in figure 11, will be accurate.*

Noise in pixel gray scale values can derive from different sources. (1) Intrinsic electronic noise. Where possible, we sought a balance between using large blocks of pixels to reduce noise and using few pixels to improve resolution. (2) Noise due to lamp fluctuations. This is subsumed within the random pixel noise measurement. (3) Variations due to fiber fluctuations in the z (optical axis) direction. Fibers may fluctuate in and out of the focal plane. With DIC optics, the dark scale magnitudes change and light and dark regions may reverse. In static situations in which no depolymerization was occurring, we saw no such shifts and therefore conclude that this is not a significant issue in our results. *This is consistent with the 1 μm or less fiber fluctuations in the focal plane. Thus, z-axis fluctuations were also small and not greater than the approximately 1 μm DIC depth of focus.*

Optics

We employed a Zeiss Axioplan microscopic with video enhanced differential (DIC) interference optics as previously described (17, 23, 27). However, instead of using a mercury

source for the transmitted, DIC, illumination we used a halogen lamp with a filter that transmits only at 680 nm and above in order to avoid undesired photolysis that a mercury arc would induce.

CO Diffusion

The potential problems arising from limitation of CO diffusion differ in the two methods we employed for inducing depolymerization. In both cases diffusion may be treated, as we have done previously (17), as occurring in two stages. In stage I solution hemoglobin that was previously deoxygenated saturates with CO. At pCO=0.3 atmosphere, this stage is rapid using the spot-shift method: as judged spectrophotometrically using transmitted light at 680 nm it is complete in 0.1 sec, sufficiently rapid that it is not a significant factor in our results. This corresponds to predicted diffusion limitation; for a 10 μm shift, the characteristic diffusion time, $t=x^2/4D$ (where, for CO, D is about $2x10^{-6}$ cm^2/sec (1)) is 0.12 sec. In our geometry it may be even faster because the CO is dropping into a well in which there is essentially no back pressure. When the method of total extinction of epi-illumination is used, stage I requires about 0.6 sec. In both cases it is unlikely that significant ligand binding to the fiber takes place during stage I because the polymer has a lower affinity for ligand than does solution hemoglobin (28, 29). In stage II the solution pCO equilibrates to its final level. The spot-shift method minimizes this stage: the amount of free CO created when the spot is moved exactly equals the amount needed to saturate the old, fiber containing, site of photolysis and no change in solution CO need occur. The principal limiting factor may arise from CO that initially diffuses in the reverse direction. On the other hand, the method of full extinction requires recruitment of solution CO from a large distance and will delay depolymerization. This delay can be observed in the low pCO points for this method in figure 12; but the effect is not large enough to alter the fundamental conclusion.

Diffusion-dependent delays arising from small deviations of a fiber from perfect linearity might be a factor in analysis of sections of a fiber for variation in depolymerizaton times. Using $t=x^2/4D$ and thus $dt/dx=x/2D$, a 1 μm displacement of a bent fiber in the presence of a 10 μm diffusion distance changes time by $\delta t=0.025$ sec (or 0.015 sec if we consider the diffusion distance, 6 μm, from the edge to the midline of the 8 μm wide spot). This deviation of ≤1 μm from the true value in half the sections would induce a shift in τ of 0.012 sec or less. Because of this and because 1 μm is the maximum deviation, it is unlikely that the $\Delta\tau$ values reported in Table II would change enough to conclude that they are due entirely to pixel-dependent noise.

This work was supported by National Institutes of Health (NHLBI) Program Project grant PO1 HL58512 (R.W.B., PI).

REFERENCES

1. Ferrone, F.A., Hofrichter, J. and Eaton, W.A. 1985a. Kinetics of sickle hemoglobin polymerization. I. Studies using temperature-jump and laser photolysis techniques. J. Mol. Biol. 183:591-610.

2. Ferrone, F.A., Hofrichter, J. and Eaton, W.A. 1985b. Kinetics of sickle hemoglobin polymerization. II. A double nucleation mechanism. J. Mol. Biol. 183:611-631.

3. Eaton, W.A. and Hofrichter, J. 1990. Sickle cell hemoglobin polymerization. Adv. Protein Chem. 40:63-279.

4. Mozzarelli, A., Hofrichter, J. and Eaton, W.A. 1987. Delay time of hemoglobin S gelation prevents most cells from sickling in vivo. Science. 237:500-506.

5. Eaton, W.A., Hofrichter, J. and Ross, P.D. 1976. Delay time of gelation: A possible determinant of clinical severity in sickle cell disease. Blood. 47(4):621-627.

6. Eaton, W.A. and Hofrichter, J. 1987. Hemoglobin S gelation and sickle cell disease. Blood. 70:1245-1266.

7. Hofrichter, J., Ross, P.D. and Eaton, W.A. 1974. Kinetics and mechanism of deoxyhemoglobin S gelation: A new approach to understanding sickle cell disease. Proc. Natl. Acad. Sci. USA. 71(12):4864-4868.

8. Moffat, K. and Gibson, Q.H. 1974. The rates of polymerization and depolymerization of sickle cell hemoglobin. Biochem. Biophys. Res. Commun. 61: 237-242.

9. Hahn, J.A., Messer, M.J. and Bradley, T.B. 1976. Ultrastructure of sickling and unsickling in time-lapse studies. Br. J. Haematol. 34(4):559-565.

10. Harrington, J.P., Elbaum, D., Bookchin, R.M., Wittenberg, J.B. and Nagel, R.L. 1977. Ligand kinetics of hemoglobin S containing erythrocytes. Proc. Natl. Acad. Sci. USA. 74(1):203-206.

11. Shapiro, D.B., Esquerra, R.M., Goldbeck, R.A., Ballas, S.K., Mohandas, N. and Kliger, D.S. 1995. Carbon monoxide religation kinetics to sickle cell hemoglobin polymers following ligand photolysis. J. Biol. Chem. 270:26078-26085.

12. Shapiro, D.B., Esquerra, R.M., Goldbeck, R.A., Ballas, S.K., Mohandas, N. and Kliger, D.S. 1996. A study of the mechanisms of slow religation to sickle cell hemoglobin polymers following laser photolysis. J. Mol. Biol. 259:947-05.

13. Shapiro, D.B., Paquette, S.J., Esquerra, R.M., Che, D., Goldbeck, R.A., Hirsch, R.E., Mohandas, N. and Kliger, D.S. 1994. Nanosecond absorption study of kinetics associated with carbon

monoxide rebinding to hemoglobin S and hemoglobin C following ligand photolysis. Biochem. Biophys. Res. Commun. 205(1):154-160.

14. Louderback, J.G., Aroutiounian, S.Kh., Kerr, W.C., Ballas, S.K. and Kim-Shapiro, D.B. 1999. Temperature and domain size dependence of sickle cell hemoglobin polymer melting in high concentration phosphate buffer. Biophys. Chem. 80:21-30.

15. Aroutiounian, S.Kh., Louderback, J.G., Ballas, S.K. and Kim-Shapiro, D.B. 2001. Evidence for carbon monoxide binding to sickle cell polymers during melting. Biophys. Chem. 91:167-181.

16. Huang, Z., Hearne, L., Irby, C.E., King, S.B., Ballas, S.K. and Kim-Shapiro, D.B. 2003. Kinetics of increased deformability of deoxygenated sickle cells upon oxygenation. Biophys. J. 85:2374-2383.

17. Agarwal, G., Wang, J.C., Kwong, S., Cohen, S.C., Ferrone, F.A., Josephs, R. and Briehl, R.W. 2002. Sickle hemoglobin fibers: mechanisms of depolymerization. J. Mol. Biol. 322:395-412.

18. Turner, M.S., Agarwal, G., Jones, C.W., Wang, J.C., Kwong, S., Ferrone, F.A., Josephs, R. and Briehl, R.W. 2006. Fiber depolymerization. Biophys. J. 91:1008-1013.

19. Dykes, G.W., Crepeau, R.H. and Edelstein, S.J. 1978. Three-dimensional reconstruction of the fibers of sickle cell hemoglobin. Nature. 272:506-519.

20. Dykes, G.W., Crepeau, R.H. and Edelstein, S.J. 1979. Three-dimensional reconstruction of 14-filament fibers of hemoglobin S. J. Mol. Biol. 130:451-472.

21. Samuel, R.E., Salmon, E.D. and Briehl, R.W. 1990. Nucleation and growth of fibers and gel formation in sickle cell hemoglobin. Nature. 345:833-835.

22. Briehl, R.W. and Guzman, A.E. 1994. Fragility and structure of hemoglobin S fibers and gels and their consequences for gelation kinetics and rheology. Blood. 83:573-579.

23. Wang, J.C., Turner, M.S., Agarwal, G., Kwong, S., Josephs, R., Ferrone, F.A. and Briehl, R.W. 2002. Micromechanics of isolated sickle cell hemoglobin fibers: bending moduli and persistence lengths. J. Mol. Biol. 315:601-615.

24. Jones, C.W., Wang, J.C., Briehl, R.W. and Turner, M.S. 2005. Measuring force between fibers by microscopy. Biophys. J. 88:2433-2441.

25. Hofrichter, J. 1986. Kinetics of sickle hemoglobin polymerization III. Nucleation rates determined from stochastic fluctuations in polymerization progress curves. J. Mol. Biol. 189:553-571.

26. Szabo, A. 1988. Fluctuations in the polymerization of sickle hemoglobin. A simple analytic model. J. Mol. Biol. 199(3):539-542.

27. Briehl, R.W. 1995. Nucleation, fiber growth and melting, and domain formation and structure in sickle cell hemoglobin gels. J. Mol. Biol. 245:710-723.

28. Hofrichter, J. 1979. Ligand binding and the gelation of sickle cell hemoglobin. J. Mol. Biol. 128:335-369.

29. Sunshine, H.R., Hofrichter, J., Ferrone, F.A. and Eaton, W.A. 1982. Oxygen binding by sickle cell hemoglobin polymers. J. Mol. Biol. 158(2):251-273.

FIGURE & TABLE LEGENDS

Figure 1. Distribution of vanishing times, based on equation (18). (a) Distribution of fiber vanishing times (expressed in terms of the dimensionless, reduced time, $s=t/\tau$, where $\tau=1/\sqrt{k\,q}$ is the characteristic time) and its dependence on the dimensionless parameter $A_o=L_o\sqrt{q/k}$ that depends on fiber length, L_o, fracture rate q, and end-depolymerization rate, k. (That higher values of A_o in this figure are associated with longer s results from the scaling of time with τ). (b) Semilogarithmic plots demonstrate the low but finite probability that fibers can exist after times much longer than the mean vanishing time. (The use of dimensionless units in this and in some other figures enables application to different conditions and time and length scales as long as A_o is not changed.). *The distributions become narrower in relation to τ (as well in absolute terms) as A_o increases (i.e. when q or L_o increase, or k decreases).*

Figure 2. Distribution of fragment lengths during depolymerization (see equations 12, 19 and 20). (a) The *mean* number of fiber fragments *within a unit length range*, *n(x)*, decreases exponentially with length and the rate of decrease is greater as time progresses. For these plots $A_o=25.8$ and $\tau=0.52$. Choosing units of seconds and microns, and with initial fiber length $L_o=10$ microns and end-depolymerization rate $k=0.75$ micron/sec, as measured in Agarwal et al (17), the fracture rate is $q=5$ events/sec per micron. These constitute values that are similar to those found under experimental conditions and *in vivo* to the extent that the latter can be estimated. (b) The same distribution is used to show the time course of fragment populations. Large fragments reach a peak early and fall off rapidly, whereas the number of small fragments undergoes lesser change.

Figure 3. Models for fiber bundle depolymerization. The rectangular blocks represent single fibers. Sections of the schematized fibers represented by a dashed lines indicate regions that have depolymerized to form gaps. For simplicity, only two or three fibers are shown for each *of the three* mechanisms *(a-c)*, but the principles may be applied to larger bundles, with magnification of the effects. (a) A bundle of two fibers that have fractured at the same location (arrow) and then end-depolymerized at the same rates. This concerted mechanism can be modeled with the same kind of equations used to describe single fiber depolymerization. (b) 2 fibers that depolymerize independently, their fractures having occurred at different times and different locations. Their mean dissolution rates and vanishing times will be the same, but fragments will not be seen until enough depolymerization has occurred to (randomly) produce gaps at the same location (arrow). Thus, the fiber bundle will appear continuous for a significant time after polymerization has commenced. (c) Interactions limit fiber fracture. In this mechanism only external fibers in a bundle can fracture. Once fracture has occurred and deeper fibers are exposed to solution, these deeper fibers can also fracture (arrow indicates incipient fracture). Under this mechanism, depolymerization will be slower than in (a) and (b) and fiber bundle continuity will be retained more than it is in (a).

Figure 4. Analytic results and Monte Carlo simulations for fiber vanishing times. Circles are Monte Carlo results of 10,550 simulations (on left ordinate). Blue line: the analytic vanishing time distribution ($Mp(s,A_o,0)$ *(where $M=10,550$)*, equation (18), scaled to number of simulations; left ordinate). Orange line: cumulative probability of vanishing ($P(s,A_o,0)$, (equation (17); right ordinate). Purple line: mean total number of fragments remaining (N, equation (14); right ordinate).

Green line: fraction of polymer remaining (L/L_o, equation (15); right ordinate). The abscissa represents vanishing time for P and Mp and time for the other parameters. Parameters for this depolymerization simulation are $q=0.001$, $k=1$, $L_o=2000$, $A_o=63.25$, $\tau=31.62$ in arbitrary units of length and time. To apply to values in the general range of experimental conditions, time and τ can be set to units of 0.01 sec as done in the figure axis, L_o to units of 0.01 micron, q to units of fractures per 0.01 micron per 0.01 sec, and k to units of .01 micron per 0.01 sec; while A_o is dimensionless and unchanged, as is s. Then $q=10$ fractures per sec per micron, $k=1$, $L=20$ microns, A_o remains 63.25 and $\tau=0.3162$ sec, corresponding to the x-axis scale in hundredths of a second..

Figure 5. Monte Carlo simulations of vanishing time distributions for different fracture rates, q. Part (a) demonstrates the large effect of fracture rate on vanishing time and also widths of the distributions. Initial fiber length is L_o=20 microns and fracture rates are per second per micron. A_o ranges from 200 for the fastest distribution to 20 for the slowest. *(b) Plotted logarithmically, the relative widths of the vanishing time distributions increase with decreasing fracture rate. At 1% of maximum the widths range from a factor of 1.8 for A_o=200 to 2.3 for A_o=20 and more for lower A_o.*

Figure 6. Part (a) shows a simulation of 10,000 characteristic times, τ, as compared to the best fit gaussian (solid line). The distribution shows marked right skewing. Mean $\tau=1.12$ with standard deviation $\Delta\tau=0.12$ and $\Delta\tau/\tau=0.11$; skewness=0.94. Parameters of the depolymerization are $L_o=10$, $q=1$, $k=1$, $\tau=1$, $A_o=10$. Part (b) shows the distribution of vanishing times in the same distribution. Mean vanishing time, $t_v=2.2$, standard deviation, $\Delta t_v=0.39$, $\Delta t_v/t_v=0.18$; skewness= 1.06. Expressed as $(\Delta t_v/t_v)/(\Delta\tau/\tau)$, the vanishing time distribution is relatively wider, but the shapes are otherwise similar and they are similarly skewed to the right.

Figure 7. Distribution of fragment lengths and mass during depolymerization. (As others, this plot can apply to different scales and values of L_o, q, and k provided A_o is unchanged). Here we use units that result in ranges encountered experimentally. Parameters are $L_o=20$ microns, $q=10$ per sec per micron, $k=1$ micron/sec, $A=63.25$, $\tau=0.3162$ second. Data are then shown as fragment lengths in hundredths of a micron and time in milliseconds, t=190 (red) and t=430 (green). (a) Fragment lengths conform to a decreasing exponential distribution whose slope becomes steeper with time. Circles indicate Monte Carlo simulations. The gray lines represent the analytic expressions (equation (12)), superposed on and essentially indistinguishable from the underlying colored lines that represent regressions of the Monte Carlo results. (b) Polymer mass associated with each fragment length exhibits a maximum and then a decrease for longer fibers. The relative mass associated with long fibers falls more rapidly at longer times. The lines superposed on the Monte Carlo data represent equation (13). The distributions are truncated at length $x=2$ microns (initial length is 20 microns) so that the mass points at $x\geq 2$ are included cumulatively in the isolated single points at $x=2$ microns. *As in figure 2, the ordinate (in a & b) gives a fragment density, expressed as the number of fragments per fiber whose length lies within a range of 1 length unit (here in microns because k and q are given in microns) at the length indicated on the abscissa*.

Figure 8. Dissolution of a fiber. Depolymerization of this 24 μm long fiber (fiber 7 in table II) was initiated by shifting the photolytic spot 10 μm to one side of the fiber, *commencing* at time approximately 1.7 sec (times are shown on the right margin). Partial pressure of CO (pCO) was 0.3 atmosphere. Frame (a) shows the fiber prior to removal of photolysis. Frame (b) shows the fiber about 1 sec after photolysis is removed. There is no discernible evidence of depolymerization. This

is consistent with the relatively flat portion of the dissolution curve associated with the shape of the progress curve as an exponential in $-(t/\tau)^2$ and/or with limited diffusion of CO to the fiber. In (c) and (d) fading of the fiber occurs. Frame (e) shows a single gap in the fiber, indicated by an arrow (see also figures 9 and 10b). In (f) through (g) fading is marked and more gaps are present along the fiber. In (h) dissolution is complete.

Figure 9. Fiber fracture. This enlargement of the section of figure 8 frame (e) indicated by the arrow shows a gap due to fiber fracture. Fiber ends at the gap are slightly displaced.

Figure 10. Fractures of the fiber in figure 8. Figure 10a shows the progress of depolymerization of the fiber as measured by the gray scale of the dark regions averaged over the fiber length as a function of time. Higher gray scale numbers indicate brighter pixels and hence less fiber. The circle corresponds to the first fracture (frame (e) in figures 8 and 10b). Figure 10b shows traces of the course of the fiber in figure 8 indicated on the ordinate in units of 1 pixel, and separated arbitrarily for clarity. Each line represents the location (transverse to the fiber) of a set (diameter, 5 pixels) of the darkest pixels at that x-axis position in the frame. Thus, for frames (a) through (d) the lines are co-linear with the fiber. In (e) there is a short section where the trace jumps upward because the fiber lacks dark pixels, indicating fracture and a gap; the darkest pixels at that cross-sectional location lie randomly at a y-axis position distant from the fiber. (The significance of the jump lies in its existence and x-axis position on the fiber. Its y-axis position and whether it is up or down have no significance. The gray scale for the deviated pixels was much lighter than that for pixels on the fiber, consistent with its representation of background pixels.) Frames (f) and (g) show the increasing presence and size of gaps. In (g) and (h) the trace of the intact fiber is superposed (in red) to facilitate identification of sites and extent of fracture. In (h) the darkest pixels are randomly located due to the absence of any fiber.

Figure 11. Different rates of dissolution in different sections of the fiber in figure 8. The course of dissolution is analyzed in 55 separate sections of 10 pixel width (44 nm/pixel) using integrated absolute values of the fiber pixel gray scales (see Methods) to obtain progress curves from which characteristic times, τ, are obtained by curve fitting. *Part (a) shows the best fit of $\exp((-t/\tau)^2)$ to the data for the entire fiber. τ=1.46 sec. The ordinate is normalized to show the fraction of polymer remaining by scaling from 1 to 0 from the start to the end of depolymerization. The abscissa scale corresponds to the times shown in figure 8 and the starting time is taken as 2.77 sec, indicated by the arrow. Part (b) shows a histogram of τ values for the 55 separately analyzed sections of the fiber. Mean τ=1.56, with the scatter standard deviation, $\Delta\tau$=0.16 sec and $\Delta\tau/\tau$=0.10. Part (c) plots τ values in sequence from beginning to end of the fiber. Much of the variation is random (independent of location on the fiber), but some may be systematic (see text). Part (d) shows the progress curves (start time is zero) and fits at the 95% confidence level for two sections, for which τ =1.19 and 1.96. The difference cannot be attributed to the pixel-dependent noise and is a function of the rates themselves. (The relative contributions of true stochastics and pixel noise more generally are analyzed in tables II and III and figure 13; see Discussion).* That rates differ among the 55 sections is consistent with the unevenness shown visually in figure 8 and by pixel analysis in figure 10.

Figure 12. Dependence of fiber fracture rate, q, on partial pressure of CO. For depolymerization induced by spot-shifting (solid red squares), the plot of characteristic time, τ,

against pCO shows a logarithmic slope of –2.34, so that fiber fracture rate $q=1/k\tau^2$ has a 4.7 power dependence on pCO. r^2 for the regression line is 0.796. For depolymerization induced by total extinction of photolytic illumination (open blue squares), possibly less accurate because of diffusion limitation, the slope is -2.88; $r^2=0.779$.

Figure 13. Simulations showing the increase in scatter of characteristic times due to random fracture in the presence of scatter due to pixel-dependent noise in images. Part (a) shows the distribution of characteristic times, τ, for 10,000 simulations of a fiber without fracture in the presence of added gaussian dark scale noise, standard deviation 0.2 on the scale of 1.0 for full fiber dissolution. The deterministic progress has the form $\exp(-(t/\tau)^2)$ before addition of noise. The best fit is then obtained after addition of noise, resulting in a range of values for τ. The distribution is closely gaussian, as judged by the best fit gaussian (solid line). Mean $\tau=1.00$, standard deviation $\Delta\tau= 0.098$, $\Delta\tau/\tau=0.088$, skewness=0.16. Part (b) shows the distribution when the original fiber is a simulation with average progress curve $\exp(-(t/\tau)^2)$, to which the same noise is added. The distribution is now wider and skewed to the right. Mean $\tau=1.12$, standard deviation $\Delta\tau= 0.156$, $\Delta\tau/\tau=0.139$, skewness=0.63. We conclude that true stochastics can be detected in the presence of noise by i) widening of the distribution compared to that for a deterministic fiber and ii) the existence of skewing. In the simulations, $\tau=1$ for both parts, (a&b,) and $L_o=10$, $q=1$, $k=1$, $A_o=10$ for part (b).

Table I: Definitions.

Table II. Experimental fibers. The table shows experimental results for fiber depolymerization carried out by removal of photolytic illumination, either by shifting of the photolytic spot or total extinction of it. Each fiber was analyzed in sections to obtain a mean value of the characteristic time, τ, and the standard deviation, $\Delta\tau$, of τ. The pixel-dependent noise, ν, was obtained by measurements on about 20 frames before depolymerization started and is expressed as a fraction of full scale depolymerization (range 1 to 0). $(\Delta\tau/\tau)/\nu$, the ratio of fractional deviation in τ to noise, was then obtained to be used in conjunction with the simulations in Table III to ascertain whether the scatter in τ, $\Delta\tau$, provides evidence of stochastics of depolymerization: if it is greater than can be explained by pixel dependent noise, it does, and if not, it dos not. Two other columns are included. The 95% confidence interval for fitting τ is usually less than the range of $\Delta\tau$, thus arguing against $\Delta\tau$ being due solely to noise-dependent fitting error. Table II also gives values of τ for each full fiber, used for figure 12, and for comparison with the mean for sections.

Table III. Simulated fibers with and without random fracture in the presence of noise. This table characterizes depolymerization simulations for a fiber depolymerizing with random fracture (top section) and compares its scatter of τ with that for a "pure" fiber that is defined (before addition of noise) by the deterministic progress curve $\exp(-(t/\tau)^2)$ (lower section). $\tau=1$ for both sections. For the fracturing fiber, $L_o=10$, $q=1$, $k=1$ and $A_o=10$. The results are shown for different levels of noise, ν. $\nu=0.2$ most closely approximates the levels in our experimental results. Because there are no intrinsic stochastics for the deterministic fiber, parameters that reflect scatter, $\Delta\tau/\tau$ and $(\Delta\tau/\tau)/\nu$, depend wholly one noise. Thus they provide a base from which stochastic scatter can be evaluated in Table II.

Table I: Definitions

x	fiber fragment length
r(x)	relative probability of fiber of length x (not normalized)
α	fracture probability at any unit site
n(x)	number of fragments of length x per unit length (i.e. in a unit length bin at x)
p(x)	probability that a fragment is of length x
N	total number of fragments
$\varphi(x)$	total mass in fragments of length x
L_o	initial fiber mass (length) before any depolymerization
L	fiber mass (length) remaining
q	breakage rate per unit length
k	end depolymerization rate (at each end)
t	time
τ	$=1/\sqrt{k\,q}$, a characteristic time
s	$=t/\tau$, dimensionless time
A_o	$= L_o\sqrt{q/k}$, a dimensionless parameter
A	$= (L_o\text{-}2kt)\sqrt{q/k}$
$\overline{N}$	mean number of fragments present
L_i	$=L_o\text{-}2kt$
$P(s,A_o,0)$	probability that no fiber is left at reduced time s
$p(s,A_o,0)$	$=\partial P/\partial s$, distribution of vanishing times (derivative of P)

Table II

Fiber	pCO	# of sections	Mean τ (of sections) (sec)	τ (whole fiber) (sec)	Δτ (sec)	Δτ /τ	Mean fitting error at 95% confidence	ν, mean std dev (before depolymerization)	Δτ /τ/ν
Spot shift									
1	0.2	55	2.022	2.367	0.294	0.146	0.169	0.201	0.726
2	0.2	55	1.857	1.315	0.305	0.164	0.199	0.172	0.955
3	0.2	55	1.755	1.736	0.312	0.178	0.149	0.135	1.318
6	0.3	55	0.930	0.842	0.155	0.167	0.065	0.132	1.259
7	0.3	55	1.561	1.460	0.159	0.102	0.083	0.117	0.868
8	0.3	55	1.661	1.294	0.213	0.129	0.178	0.208	0.617
12	0.4	55	0.355	0.417	0.082	0.231	0.048	0.120	1.928
13	0.4	55	0.361	0.277	0.038	0.105	0.043	0.135	0.781
14	0.4	54	0.328	0.225	0.104	0.317	0.044	0.136	2.331
15	0.4	54	0.302	0.304	0.048	0.159	0.058	0.202	0.786
19	0.5	68	0.321	0.320	0.075	0.232	0.061	0.200	1.159
Average			1.041	0.960	0.162	0.175	0.100	0.160	1.157
Std			0.695	0.689	0.100	0.060	0.058	0.035	0.513
Epi-illumination off									
4	0.3	17	4.177	2.942	1.587	0.380	0.305	0.245	1.552
5	0.3	29	2.207	2.544	0.909	0.412	0.173	0.197	2.095
9	0.4	66	0.667	0.568	0.041	0.062	0.074	0.080	0.773
10	0.4	43	0.678	0.324	0.068	0.101	0.078	0.110	0.916
11	0.4	43	0.679	0.299	0.074	0.109	0.067	0.091	1.203
16	0.5	35	0.404	0.329	0.072	0.177	0.066	0.179	0.989
17	0.5	45	0.463	0.371	0.058	0.125	0.060	0.127	0.983
18	0.5	52	0.296	0.28	0.055	0.186	0.059	0.214	0.870
20	0.8	10	0.187	0.185	0.033	0.176	0.030	0.165	1.067
21	0.8	15	0.091	0.074	0.018	0.195	0.023	0.217	0.899
Average			0.985	0.792	0.292	0.192	0.094	0.162	1.135
Std			1.204	0.987	0.502	0.110	0.080	0.054	0.381

Table III

Noise, ν	Mean τ	Δτ	Δτ /τ	Δτ /τ/ν
Fiber with random fracture				
0	0.9978	0.1068	0.107	--
0.01	0.9958	0.1048	0.1053	10.527
0.1	0.997	0.1168	0.1171	1.1712
0.2	0.9942	0.1387	0.1395	0.6974
0.3	0.9987	0.1874	0.1876	0.6254
Fiber without stochastics				
0	1	0	0	--
0.01	1.0001	0.0047	0.0047	0.4656
0.1	1.0005	0.0464	0.0463	0.4634
0.2	1.0024	0.0922	0.092	0.4598
0.3	1.0038	0.1407	0.1401	0.4671

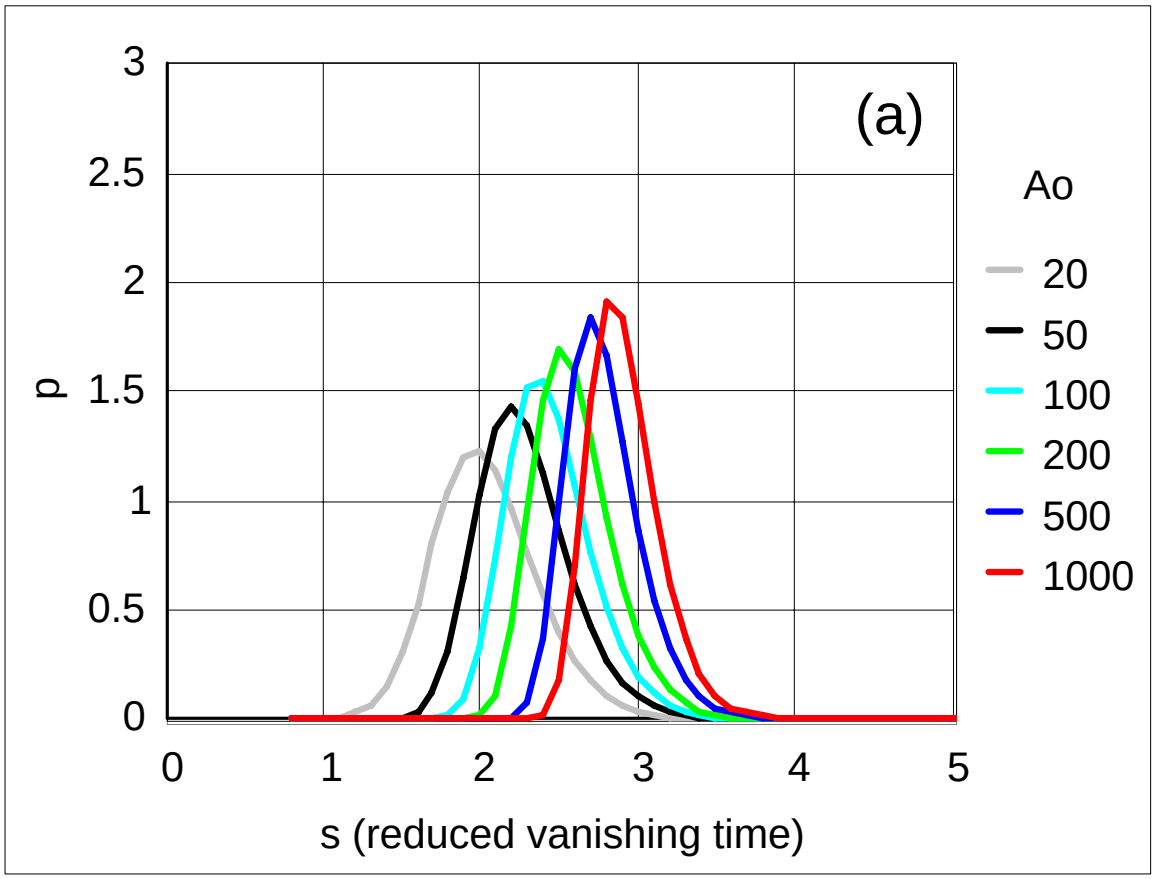

Wang: figure 1(a)

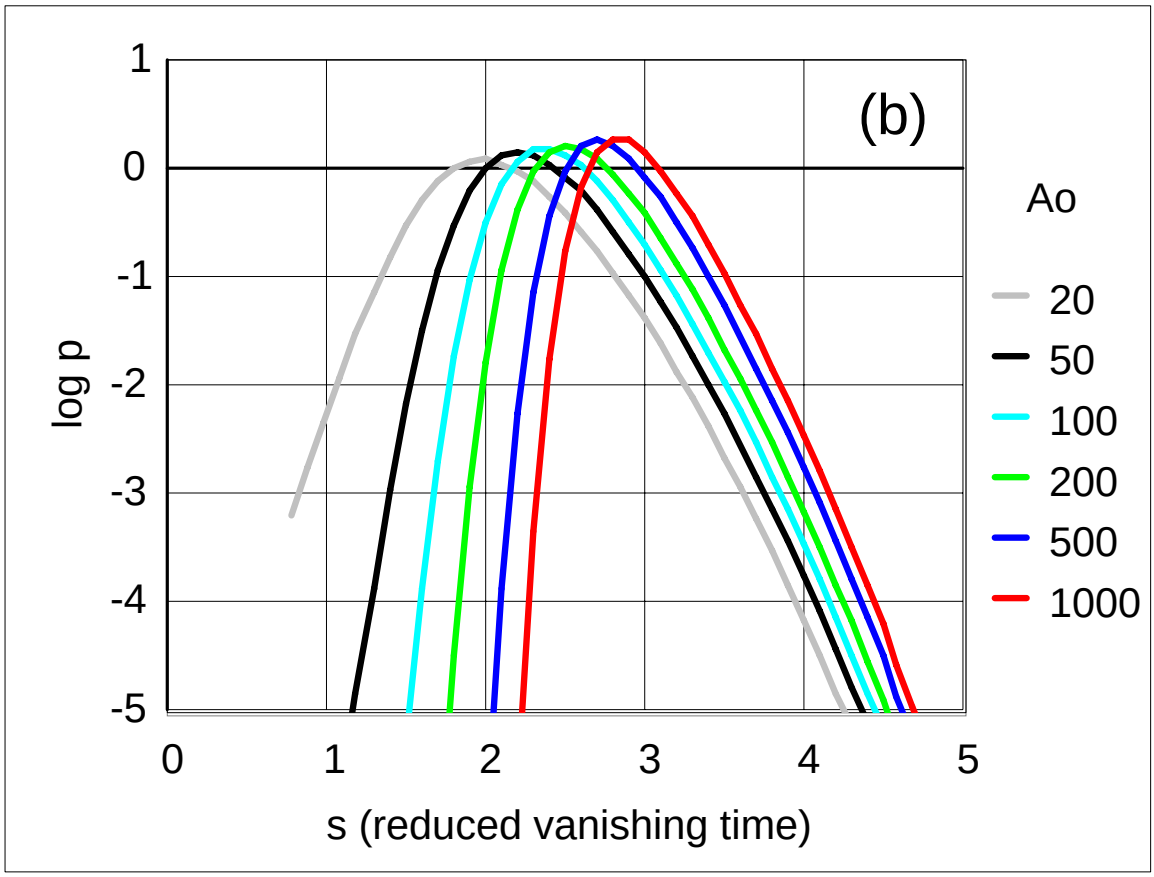

Wang: figure 1(b)

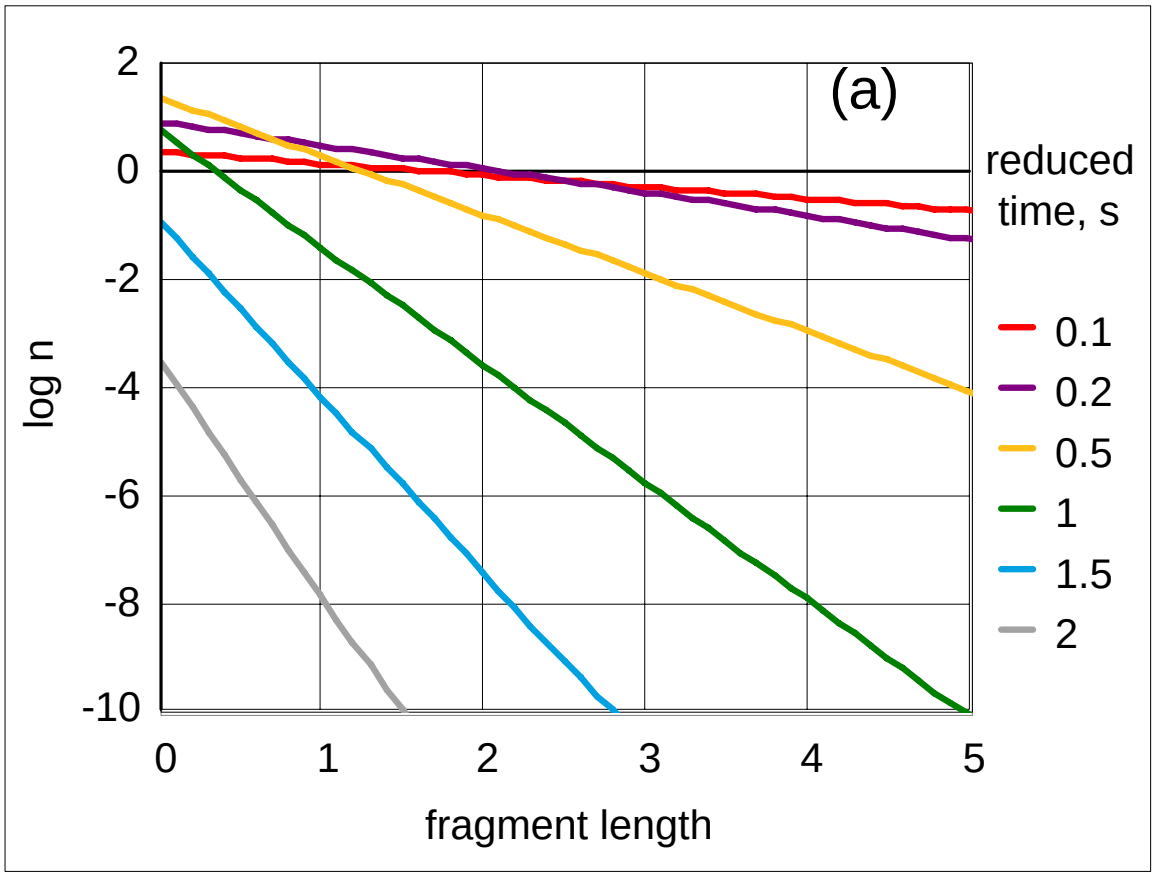

Wang: figure 2(a)

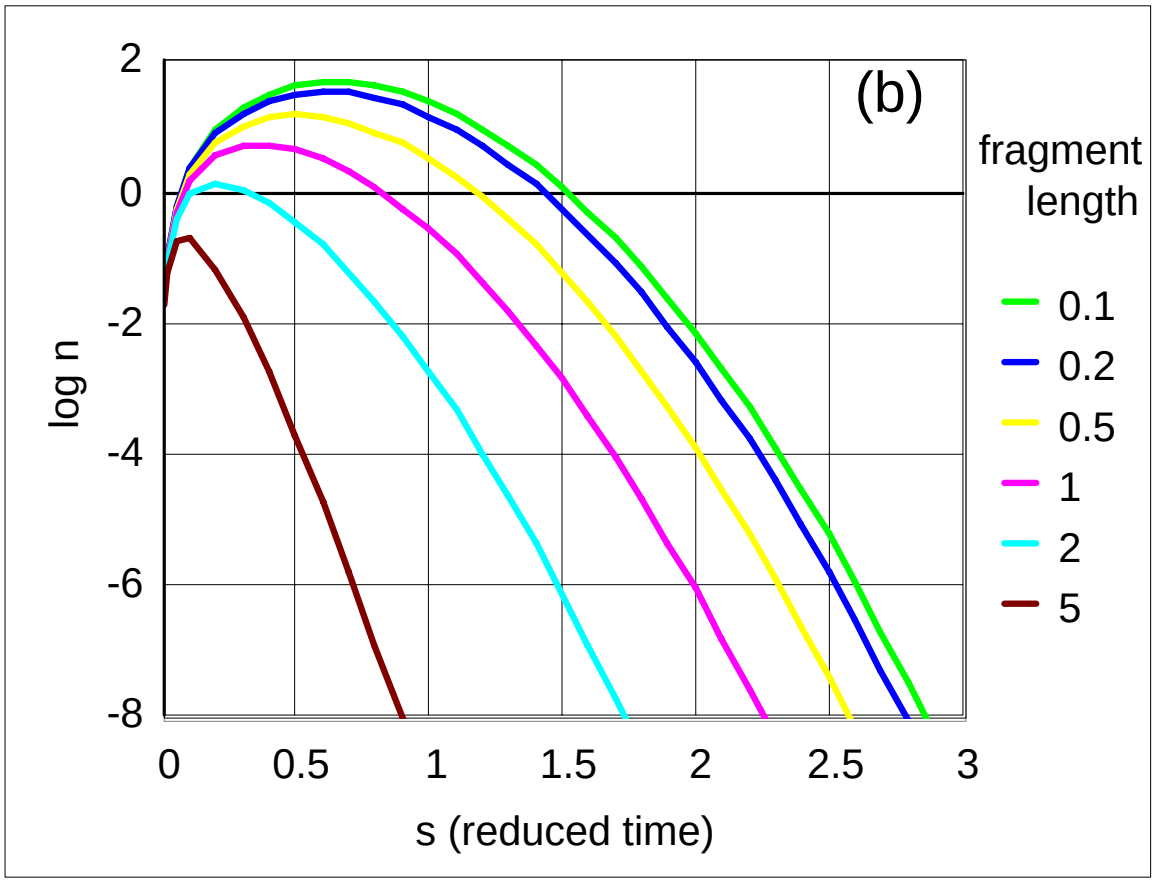

Wang: figure 2(b)

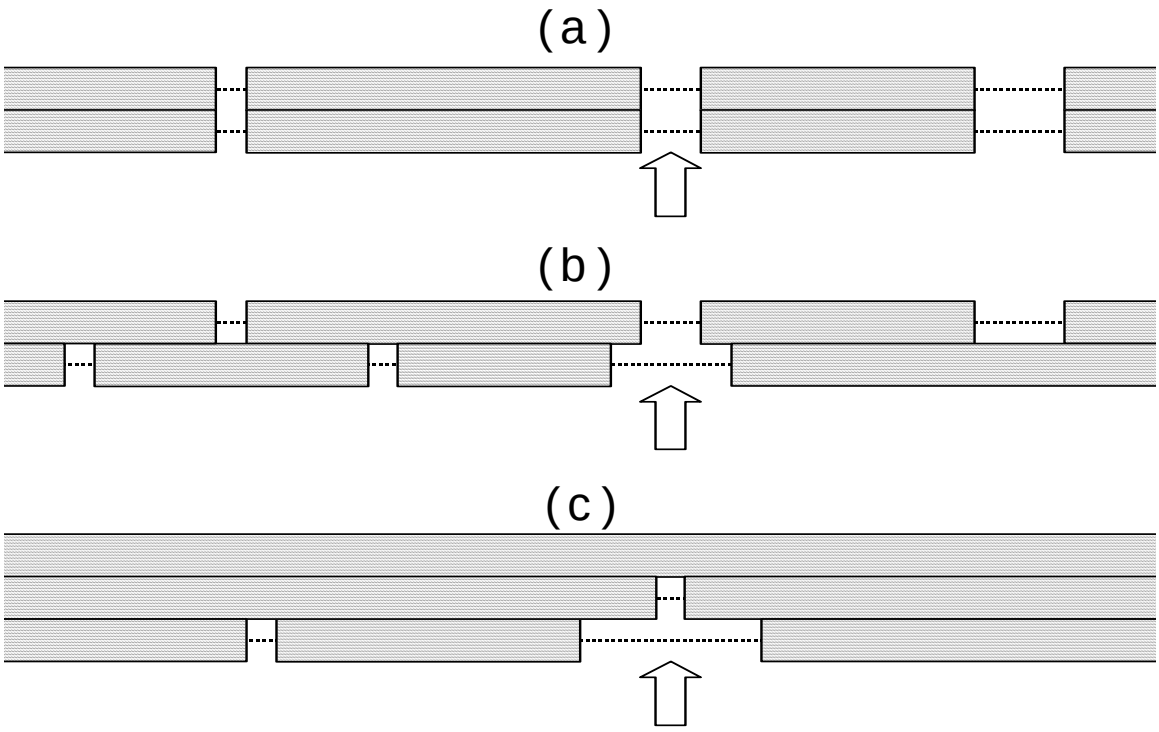

Wang: figure 3

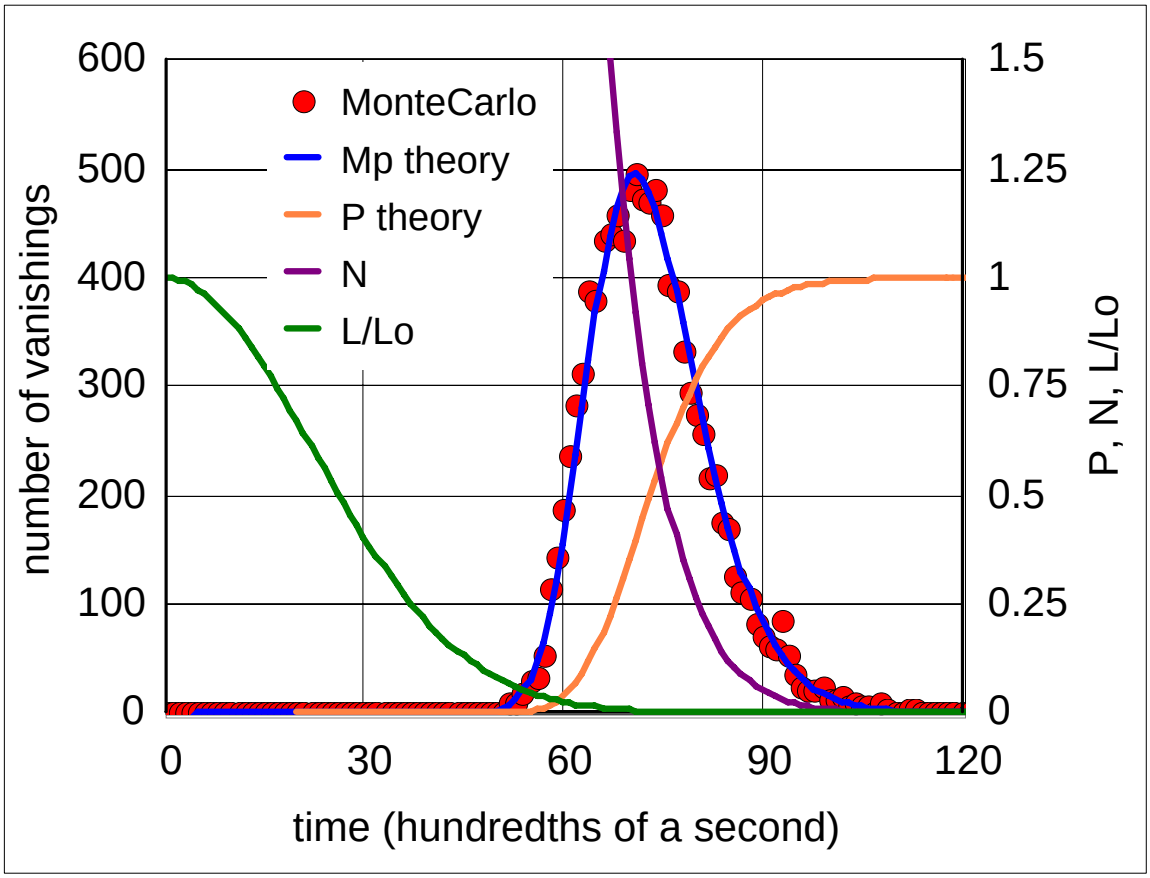

Wang: figure 4

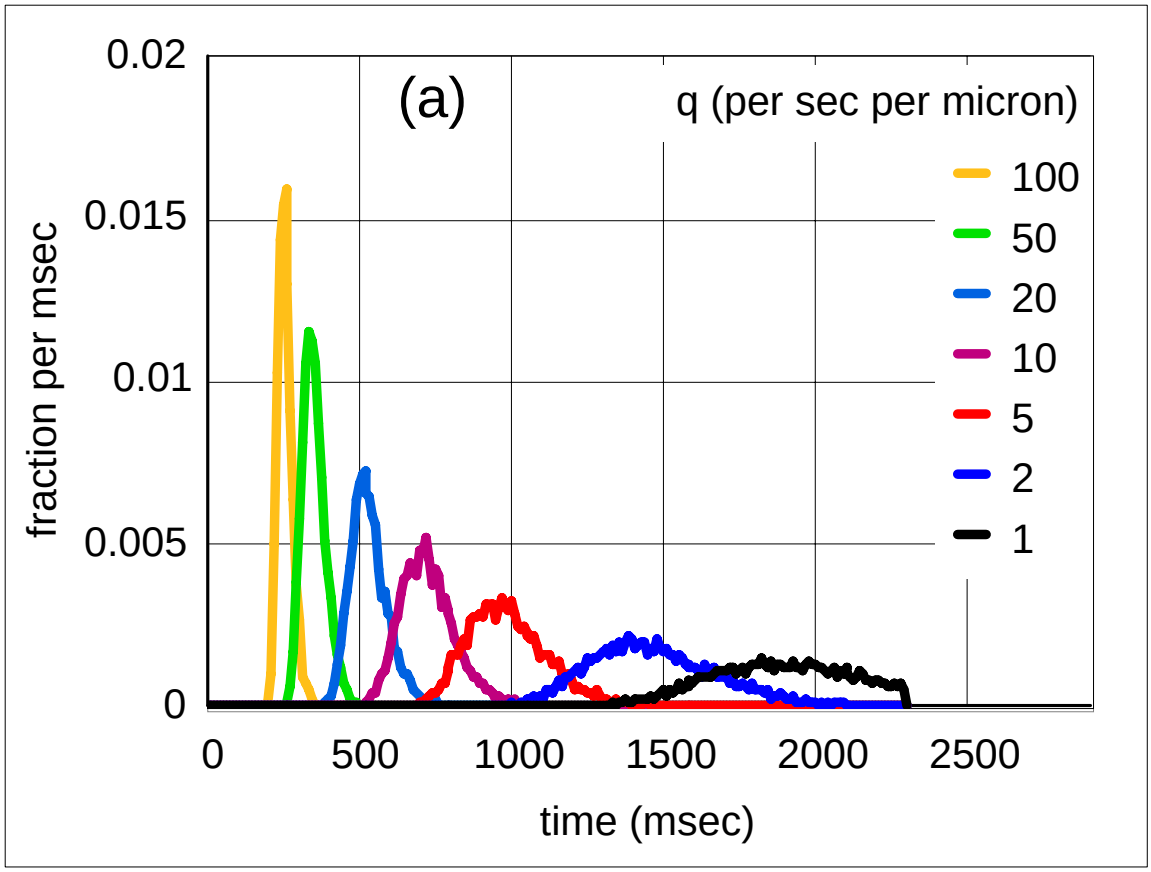

Wang: figure 5(a)

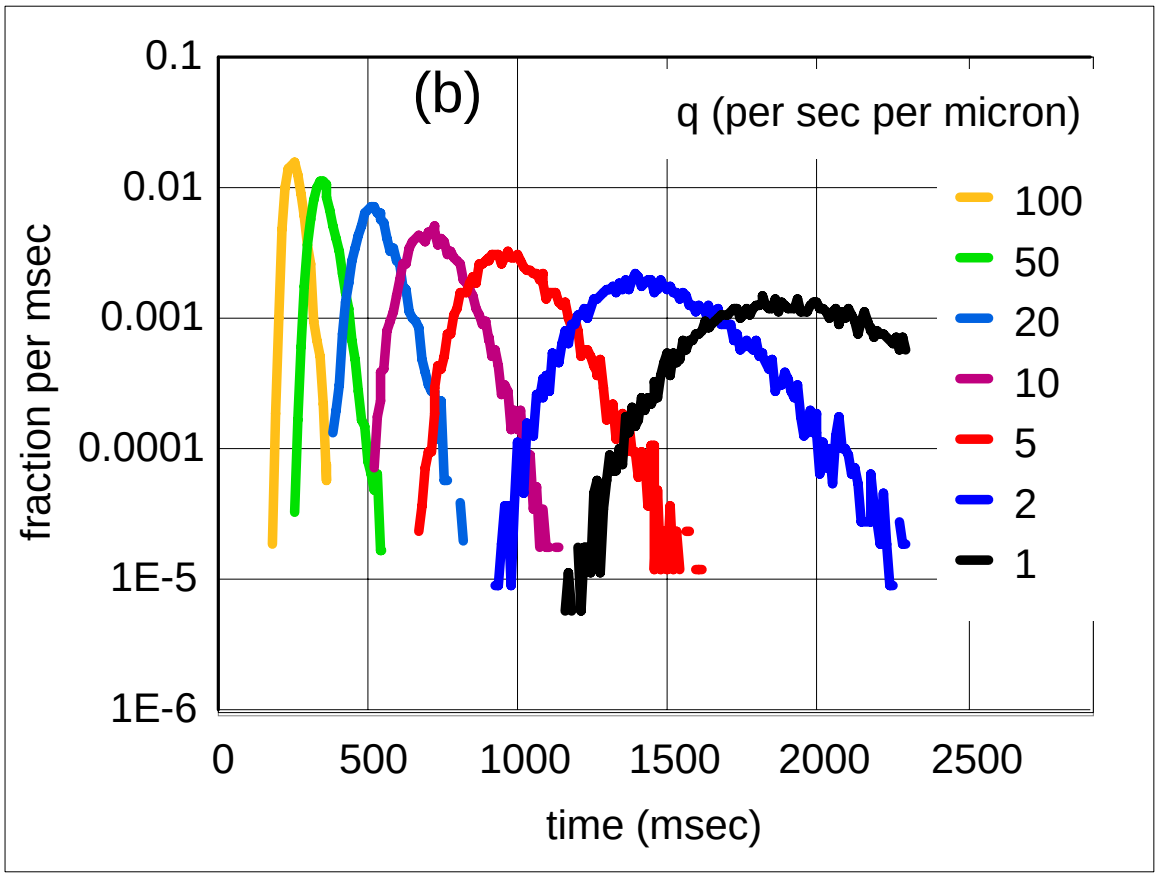

Wang: figure 5(b)

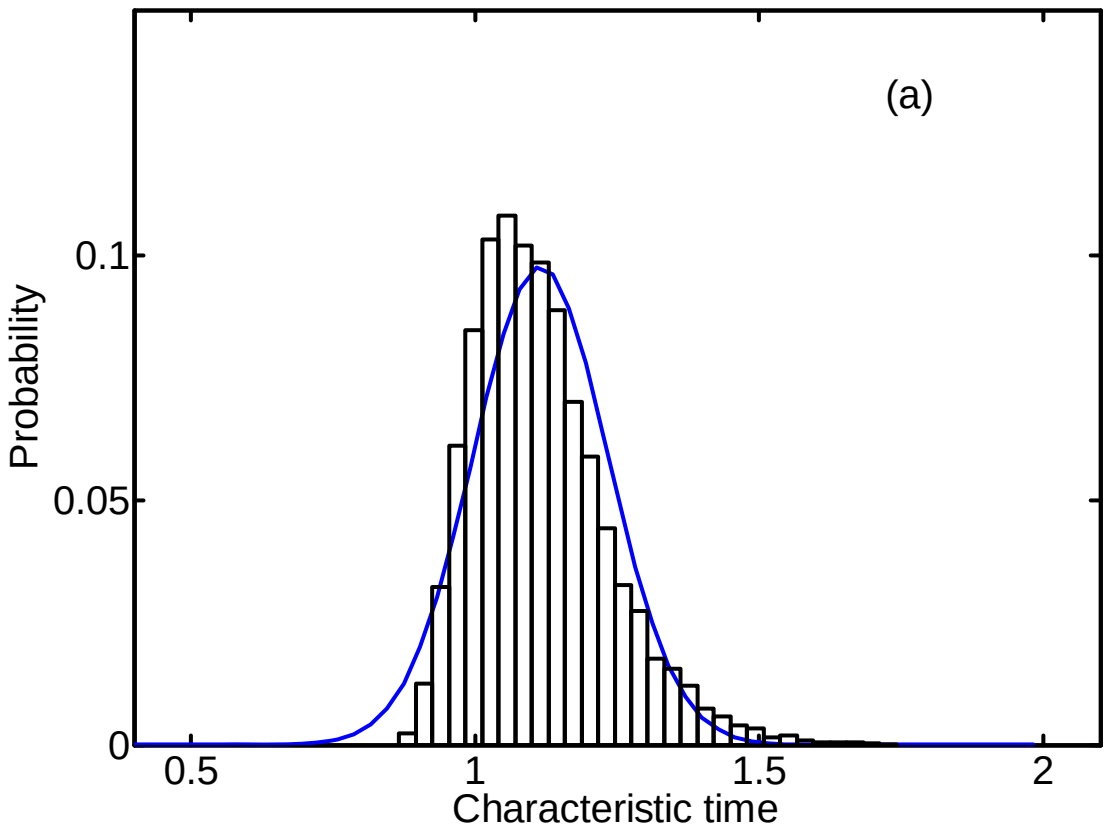

Wang: figure 6(a)

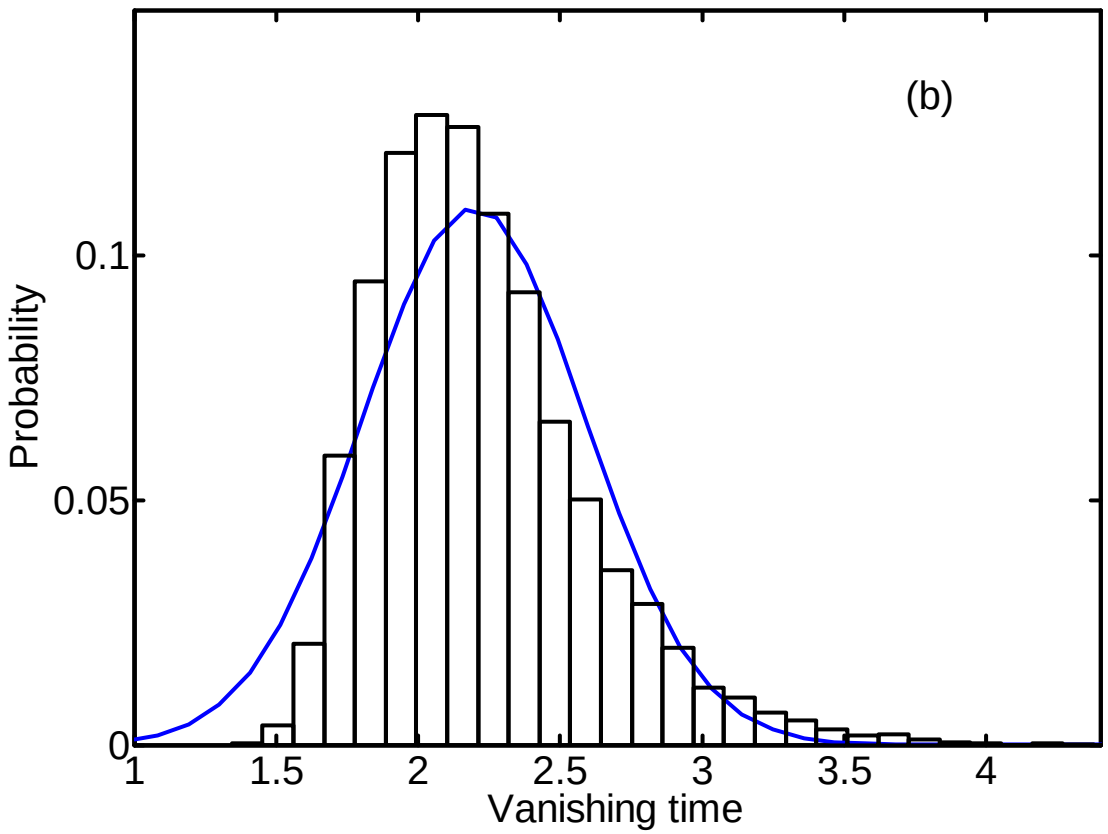

Wang: figure 6(b)

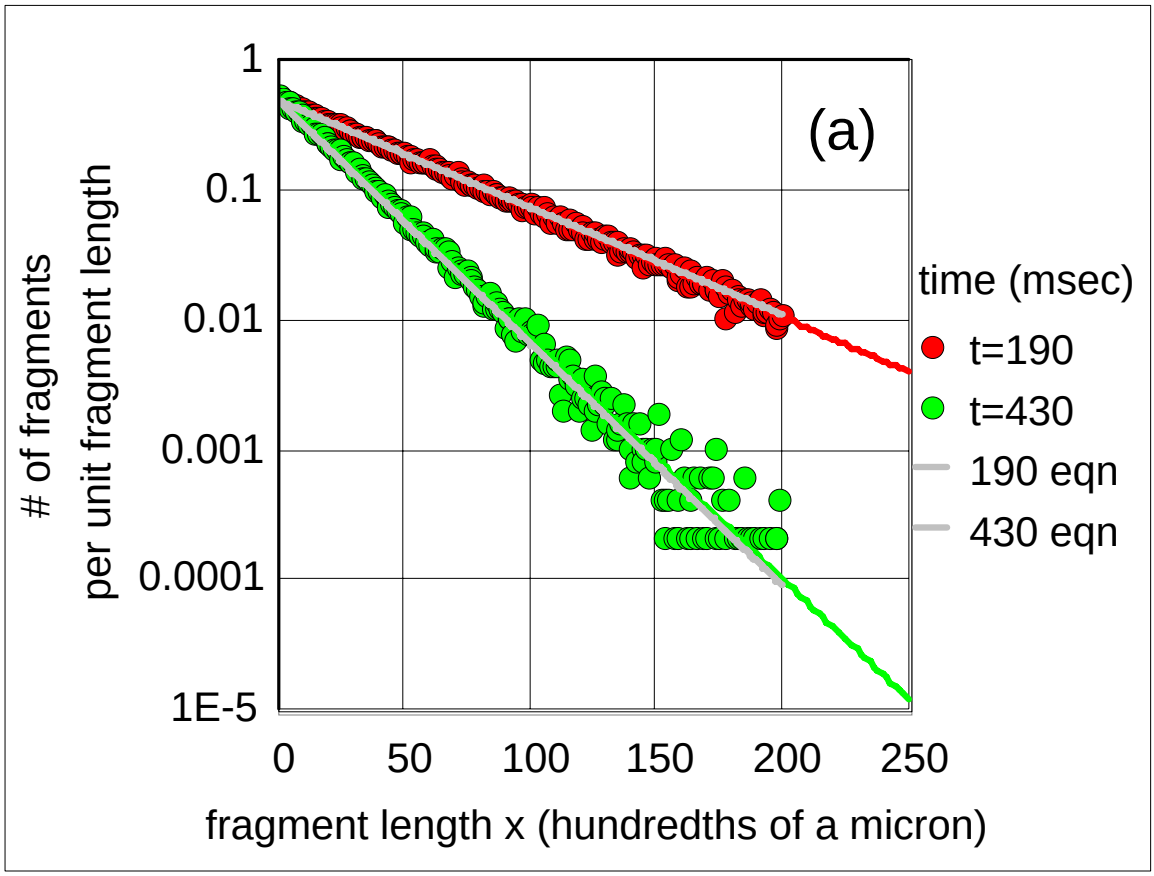

Wang: figure 7(a)

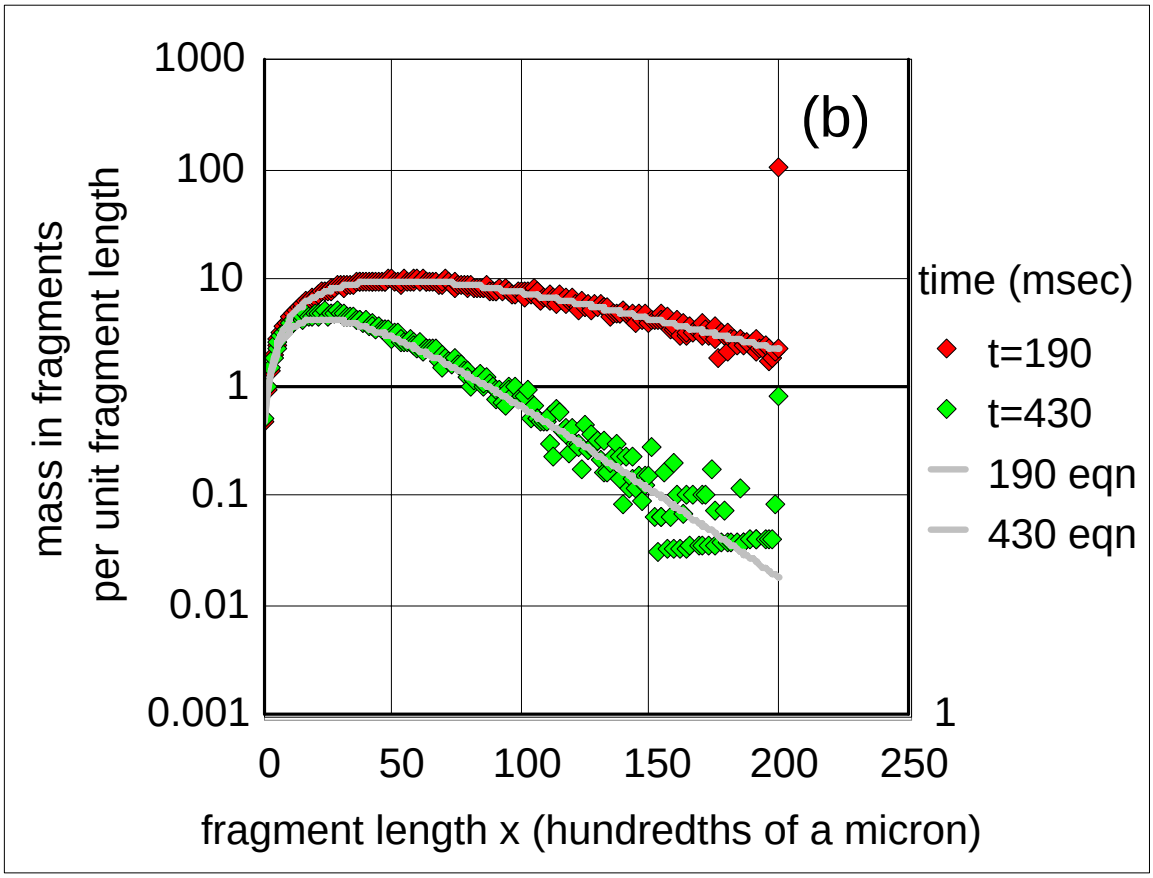

Wang: figure 7(b)

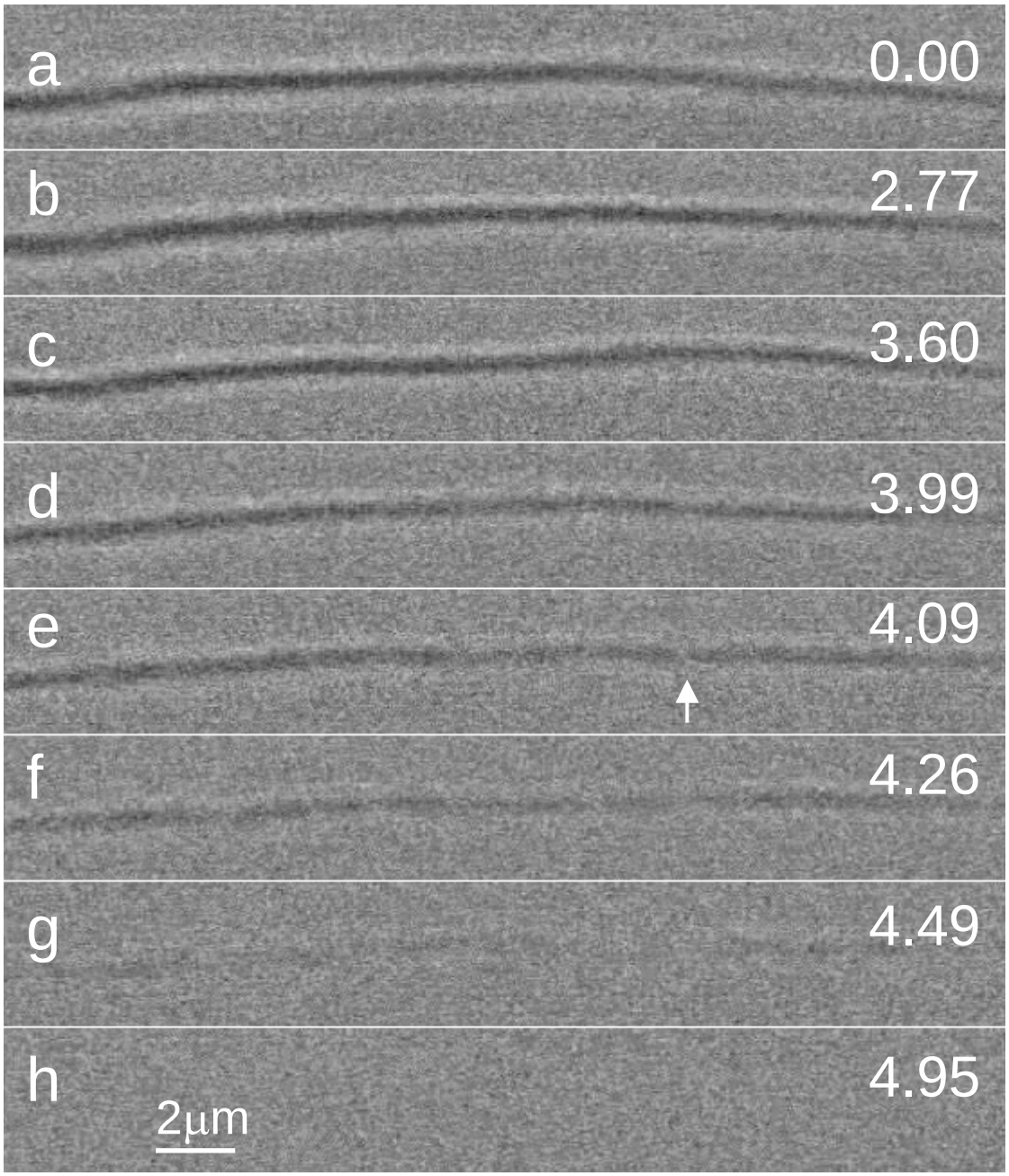

Wang: figure 8

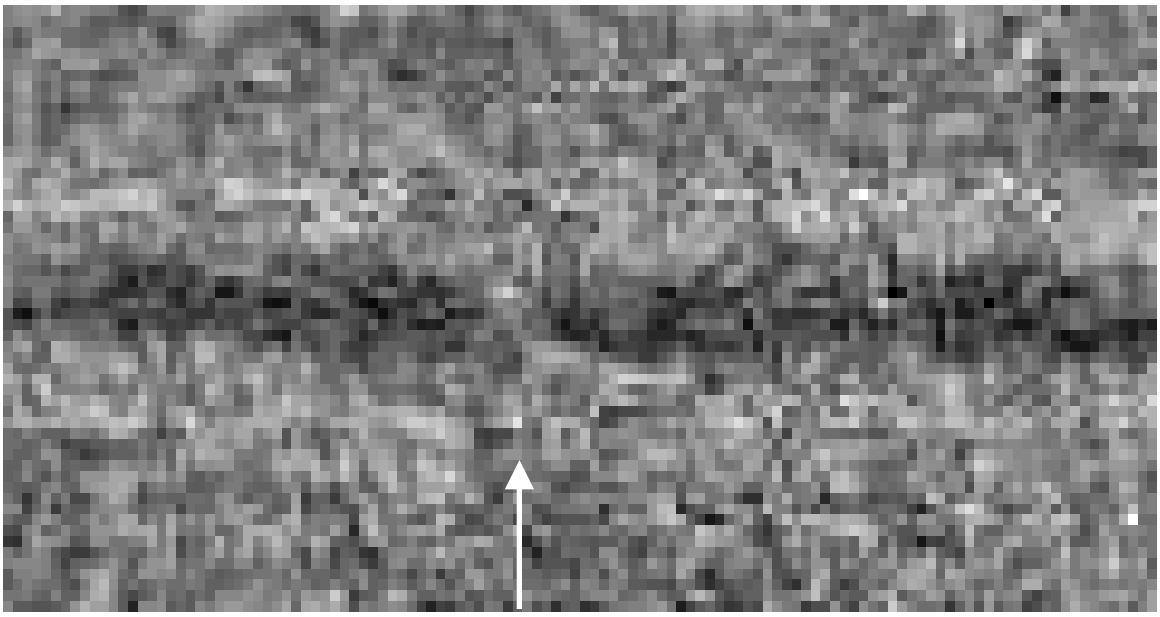

Wang: figure 9

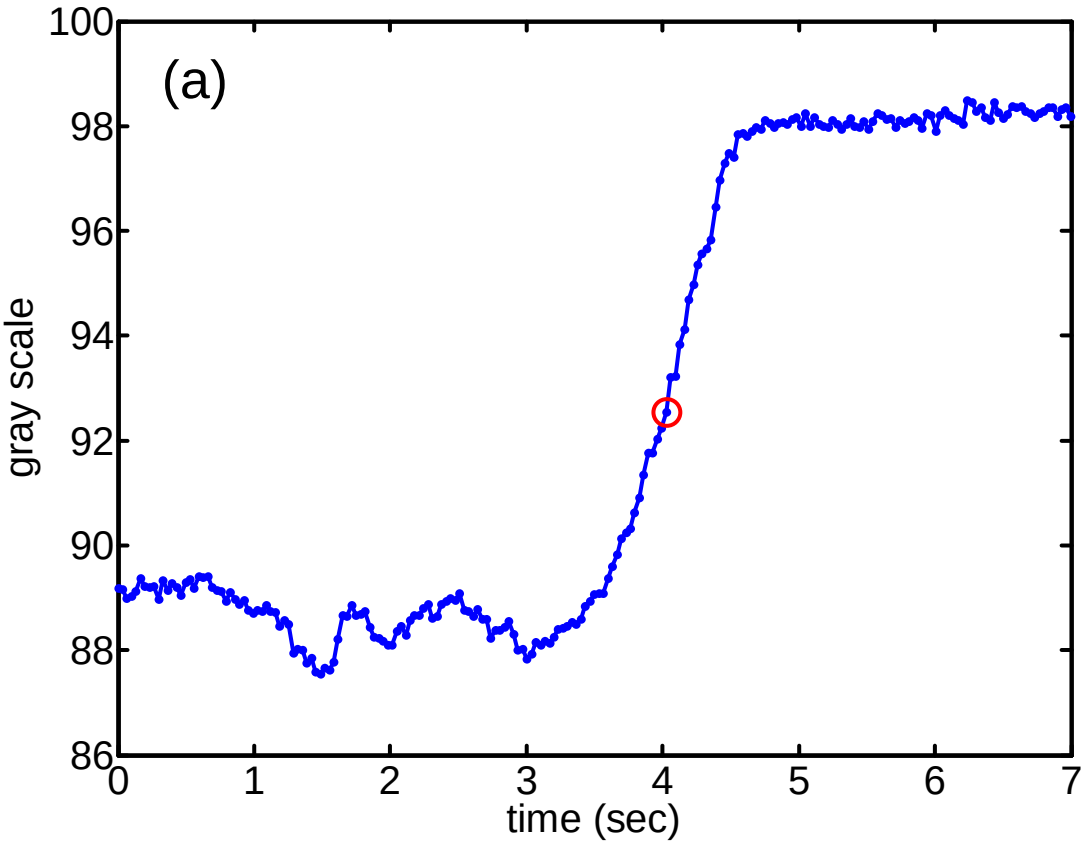

Wang: figure 10(a)

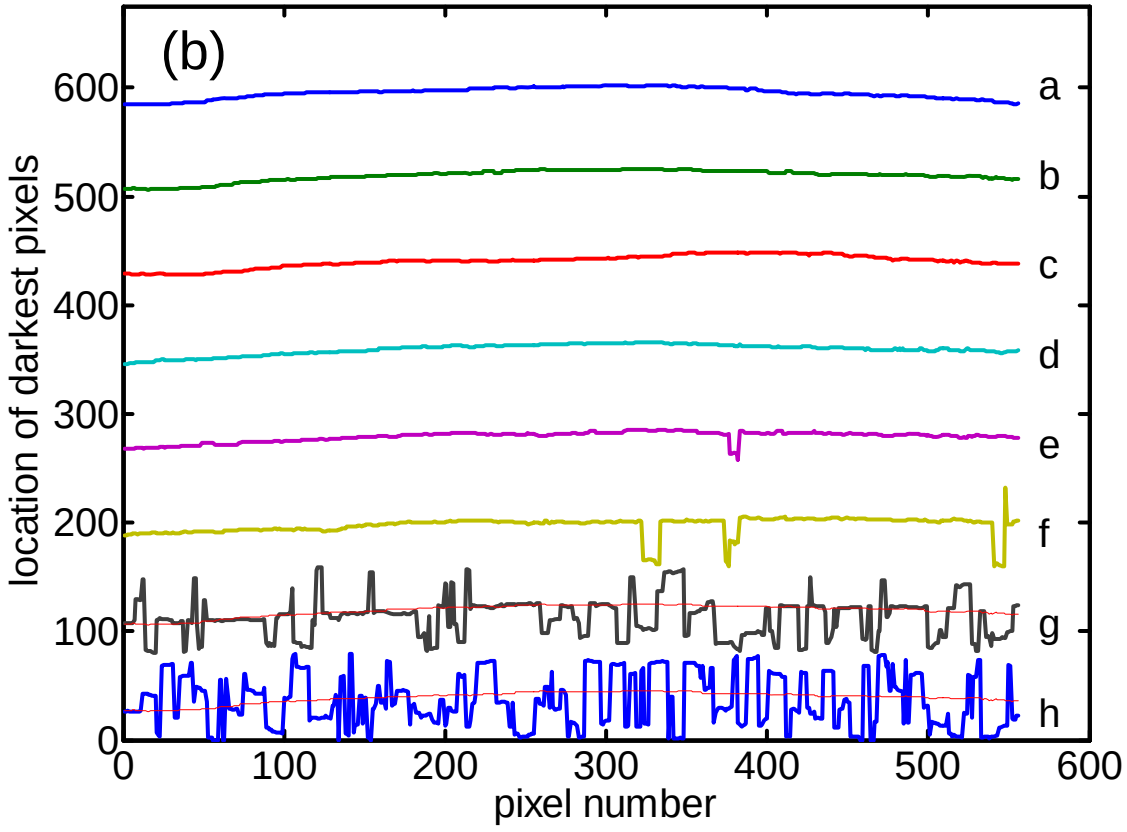

Wang: figure 10(b)

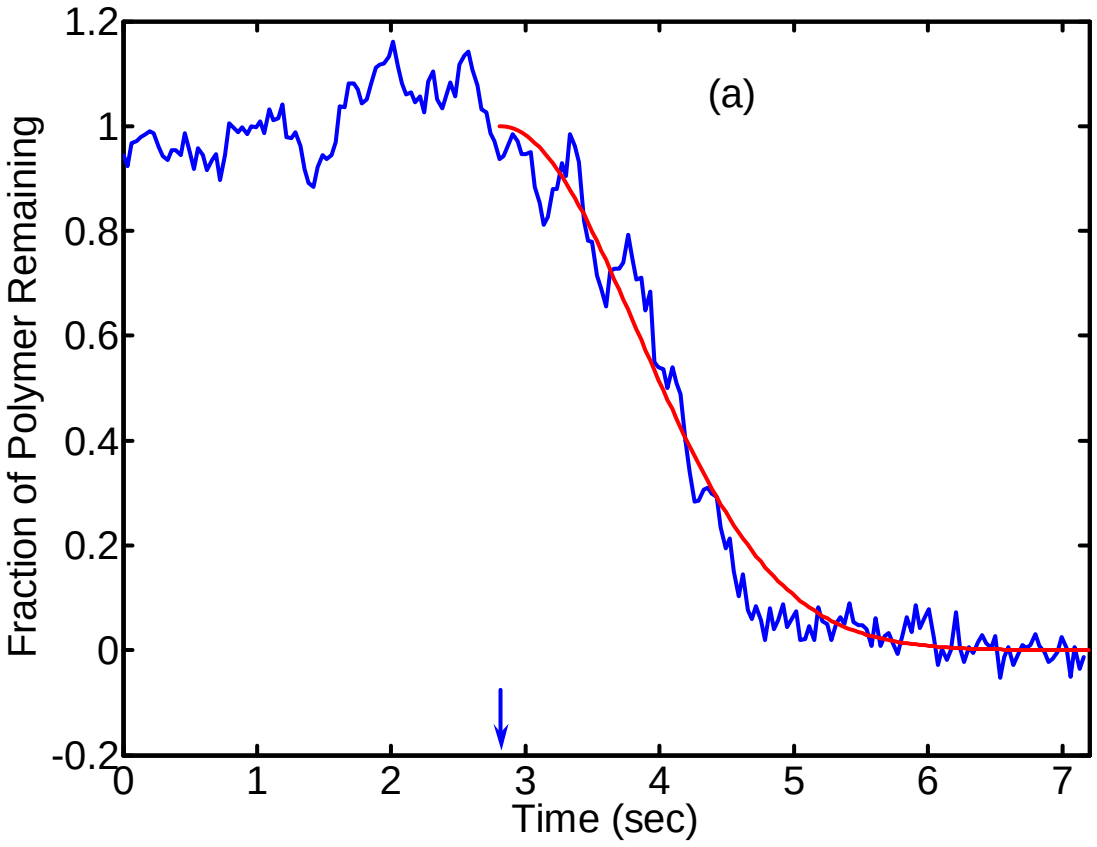

Wang: figure 11(a)

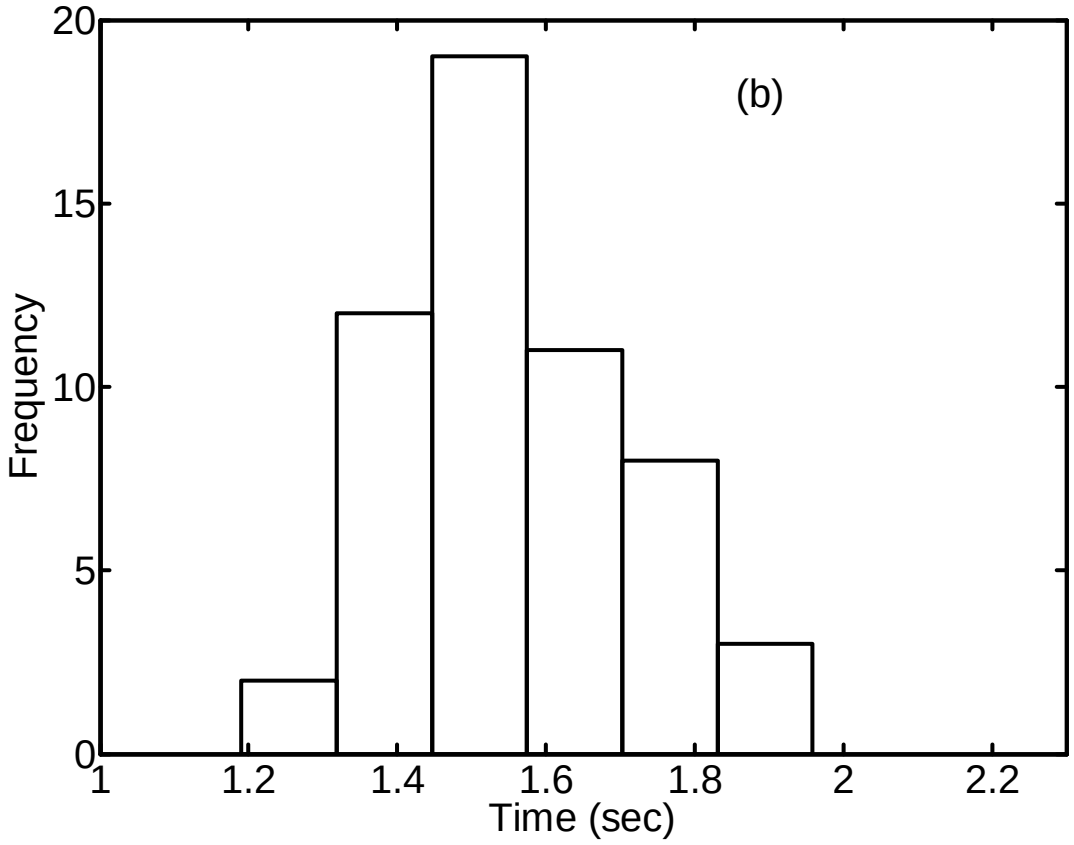

Wang: figure 11(b)

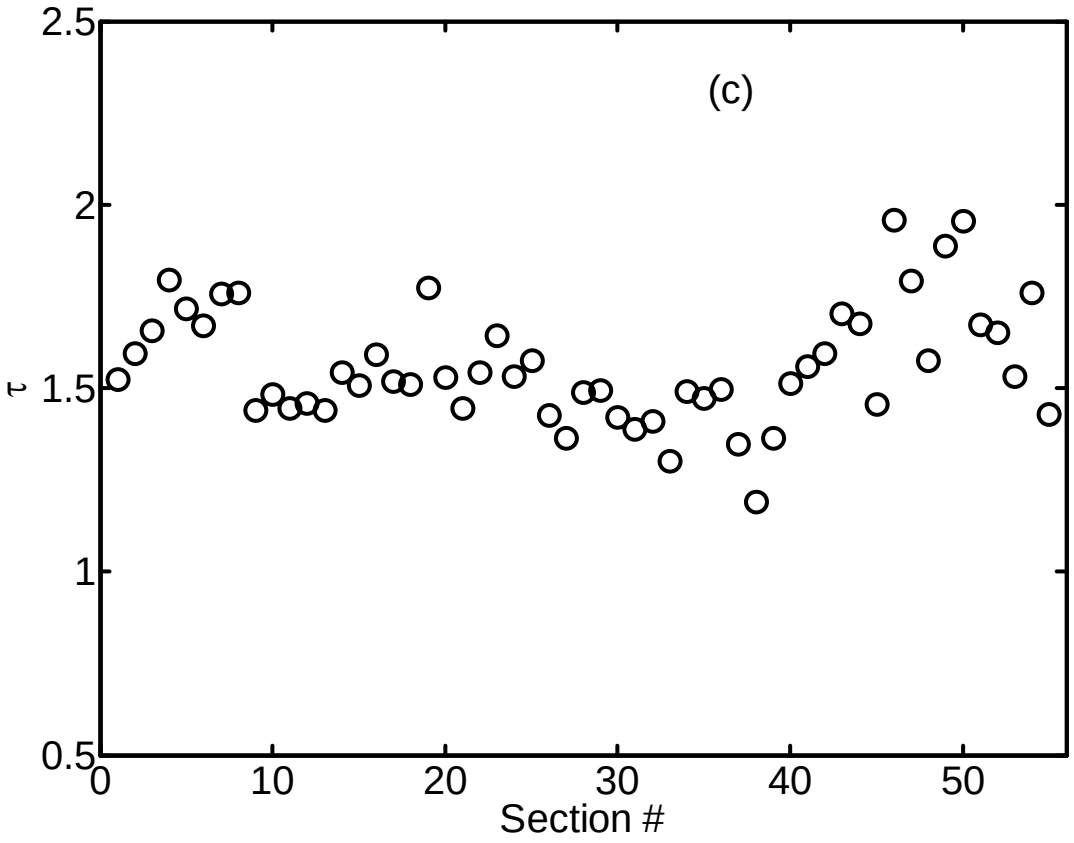

Wang: figure 11(c)

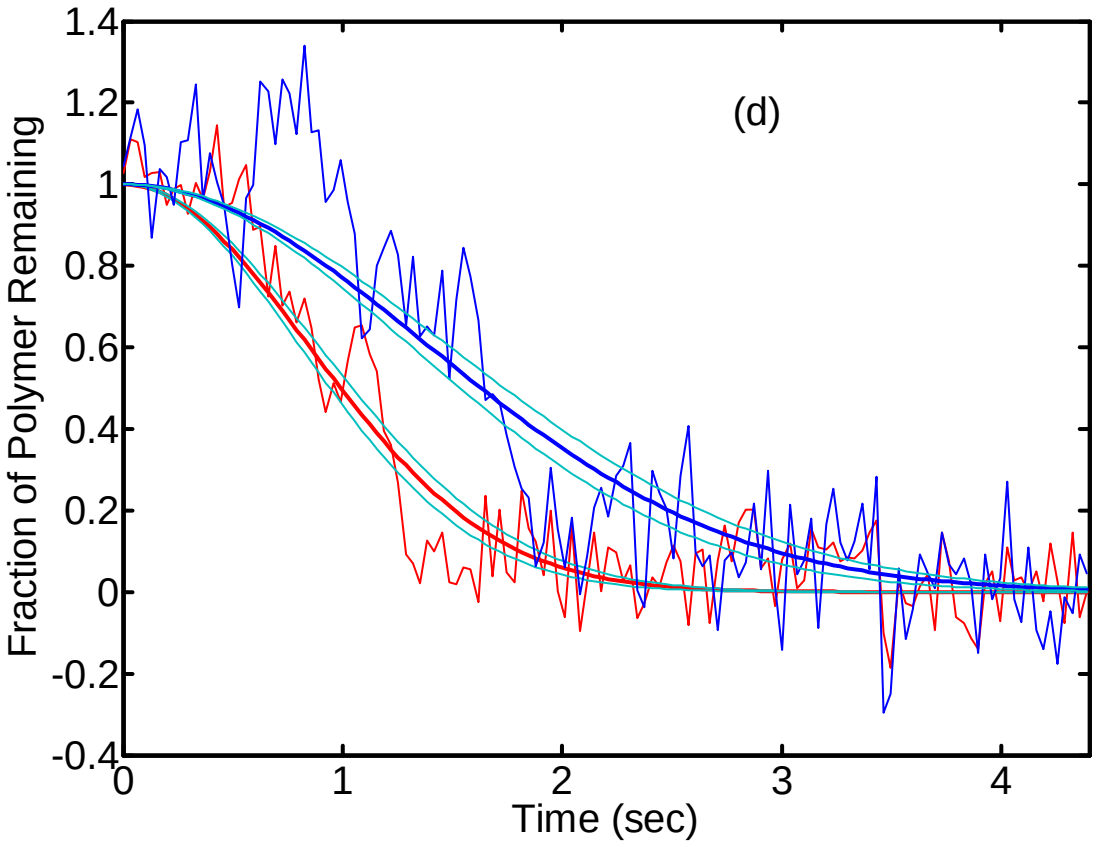

Wang: figure 11(d)

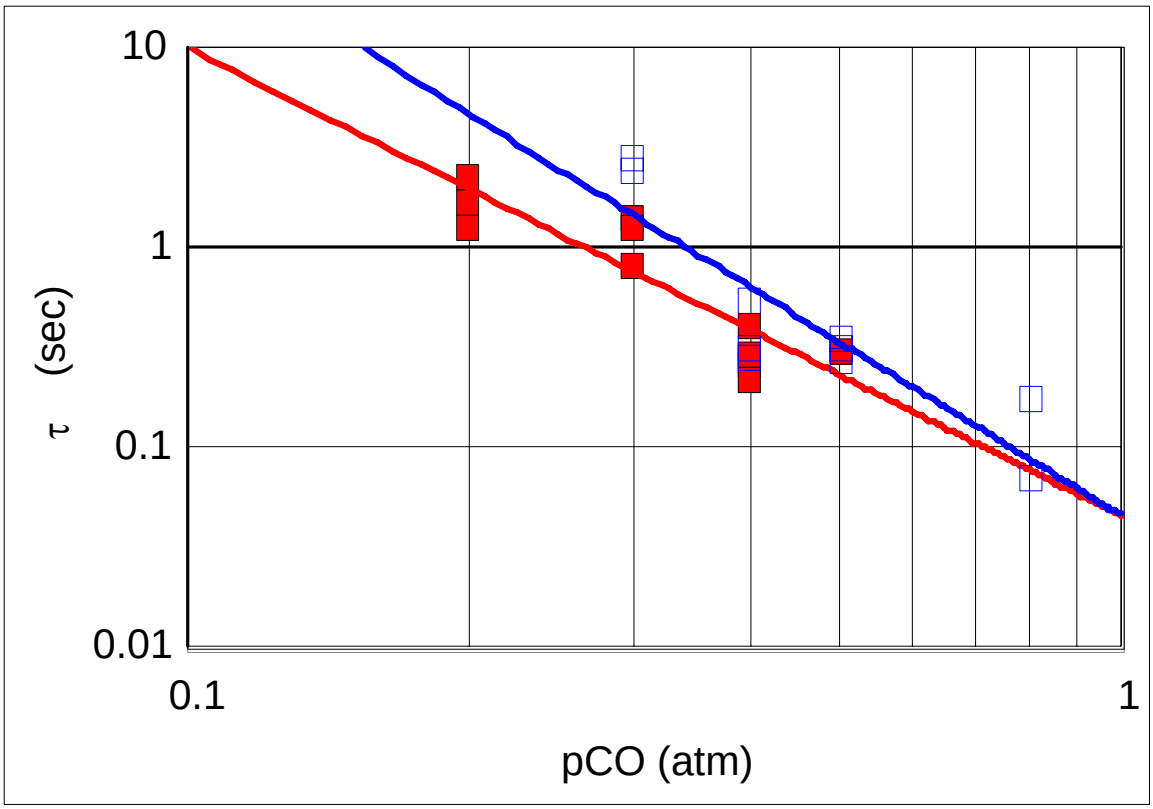

Wang: figure 12

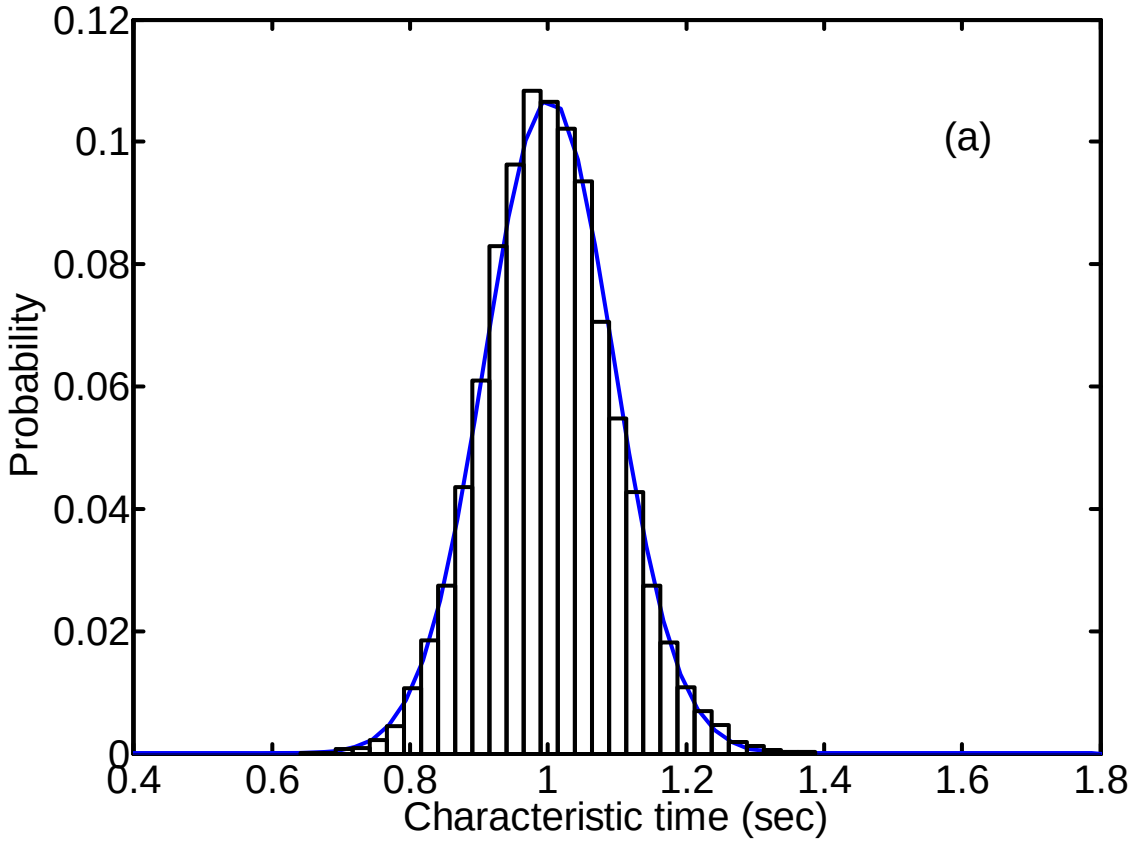

Wang: figure 13(a)

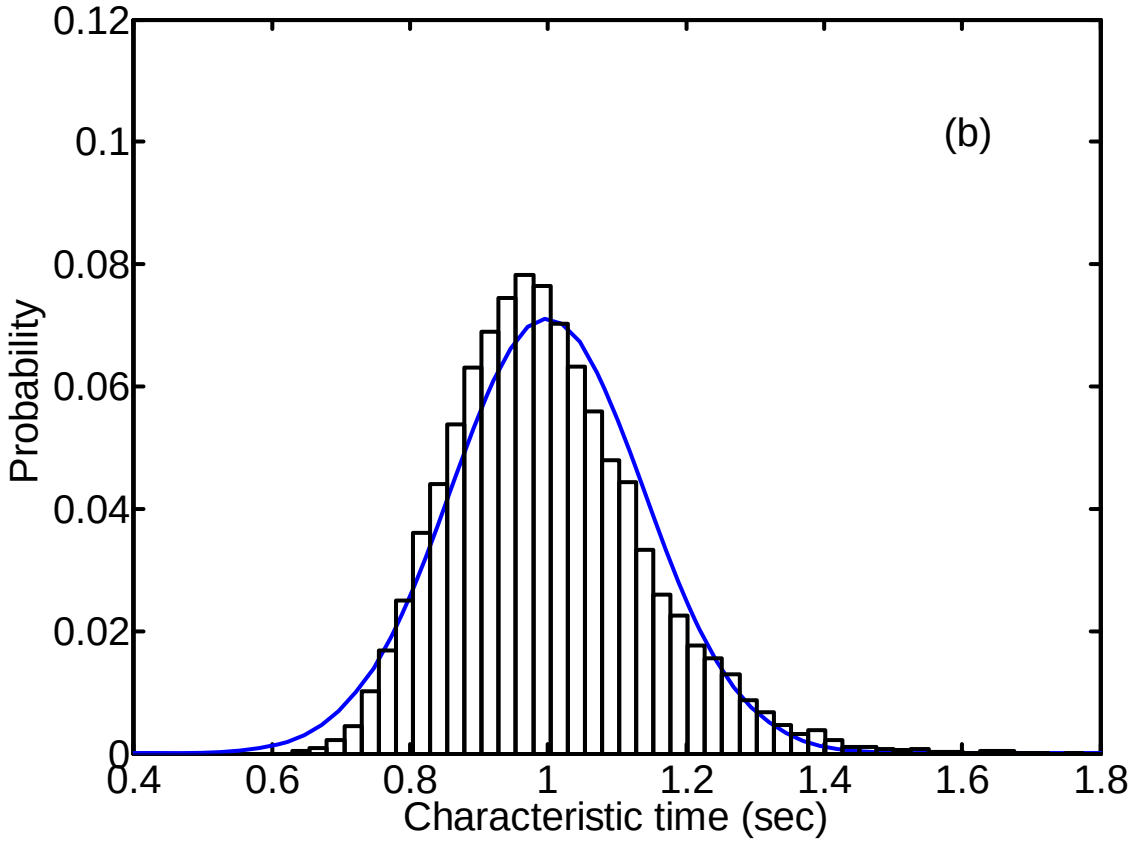

Wang: figure 13(b)